EFDA–JET–PR(13)45

D. Testa, H. Carfantan, M. Albergante, P. Blanchard, A. Fasoli, A. Goodyear,
A. Klein, J.B. Lister, T. Panis and JET EFDA contributors

Sparse Representation of Signals: From Astrophysics to Real-time Data Analysis for Fusion Plasmas and System Optimization Analysis for ITER

Sparse Representation of Signals: From Astrophysics to Real-time Data Analysis for Fusion Plasmas and System Optimization Analysis for ITER

D. Testa[1], H. Carfantan[2], M. Albergante[3], P. Blanchard[1,4], A. Fasoli[1], A. Goodyear[5], A. Klein[6], J.B. Lister[1], T. Panis[3] and JET EFDA contributors*

JET-EFDA, Culham Science Centre, OX14 3DB, Abingdon, UK

[1]Ecole Polytechnique Fédérale de Lausanne (EPFL), Centre de Recherches en Physique des Plasmas (CRPP), Association EURATOM – Confédération Suisse, Lausanne, CH
[2]Université de Toulouse, Institut de Recherche en Astrophysique et Planétologie, Centre National pour la Recherche Scientifique, Toulouse, France
[3]Centre de Recherches en Physique des Plasmas (CRPP), EPFL, Lausanne, CH
[4]EFDA-CSU, Culham Science Centre, Abingdon, UK
[5]EURATOM-CCFE Fusion Association, Culham Science Centre, OX14 3DB, Abingdon, OXON, UK
[6]Plasma Science and Fusion Centre, Massachusetts Institute of Technology, Boston, USA
** See annex of F. Romanelli et al, "Overview of JET Results", (24th IAEA Fusion Energy Conference, San Diego, USA (2012)).*

Preprint of Paper to be submitted for publication in
Plasma Physics and Controlled Fusion

ABSTRACT

Efficient, real-time and unsupervised data analysis is one of the key elements for achieving scientific success in complex engineering and physical systems, of which two examples are the JET and ITER tokamaks.

There is a wealth of signal processing techniques that are being applied to post-pulse and real-time data analysis in such complex systems, and here we wish to present some examples of the synergies that can be exploited when combining ideas and methods from different fields, such as astronomy and astrophysics and thermonuclear fusion plasmas.

One problem which is common to these subjects is the determination of pulsation modes from irregularly sampled time-series. We have used recent techniques of signal processing in astronomy and astrophysics, based on the Sparse Representations of Signals, to solve current questions arising in thermonuclear fusion plasmas. Two examples are the detection of magneto-hydrodynamic instabilities, which is now performed routinely in JET in real-time on a sub-millisecond time-scale, and the studies leading to the optimization of the magnetic diagnostic system in ITER. These questions have been solved formulating them as inverse problems, despite the fact that these applicative frameworks are extremely different from the classical use of Sparse Representations, on both the theoretical and computational points of view.

Requirements, prospects and ideas for the signal processing and real-time data analysis applications of this method to routine operation of ITER will also be discussed.

1. INTRODUCTION.

Efficient, real-time and unsupervised data analysis is one of the key elements for achieving scientific success in complex engineering and physical systems, of which two examples are the JET and ITER tokamaks. There is a wealth of signal processing techniques that are being applied to data analysis in such complex systems, and here we wish to present some examples of the synergies that can be exploited when combining ideas and methods from different fields, such as astronomy and astrophysics and thermonuclear fusion plasmas.

One problem which is common to these subjects is the determination of pulsation modes from irregularly sampled temporal and spatial series [1]. Historically, this problem has been addressed combining methods based on various forms of the Fourier Transforms for the time-series analysis, and using methods essentially based around the Lomb-Scargle periodograms [2-5] for the spatial-series analysis. For the latter, much work has been performed to improve on the limitations of the original periodogram methods, essentially in the field of Astronomy and Astrophysics (A&A). This general measurement problem is further complicated in thermonuclear fusion plasmas, and specifically in large-scale tokamak and stellarator devices, by the (often very) low number of measurement points in the spatial domain, which is due to in-vessel engineering and installation constraints, leading to a number of mathematical difficulties. Therefore, analysis method based on the spatial Nyquist criterion cannot in general be used because of the effect of aliasing, particularly if intermediate to

small wavelengths need to be resolved. For the specific case of magneto-hydro-dynamic (MHD) instabilities in tokamak devices, this deficiency has prompted the development and the successful application of various analysis methods, such as the Singular Value (SVD) [6, 7] and wavelet [8] decompositions, the Wigner [9], Choi-Williams [10, 11] and Hilbert [12] Transforms, and a generalization of the Lomb-Scargle periodograms [12].

A particular sub-class of MHD analysis problems is that of understanding the behaviour of instabilities that are essential for controlling the stability of magnetically confined thermonuclear plasmas. Specifically, the problem of unsupervised real-time detection of MHD modes has now become one of the most important aspects for machine protection and control of plasma discharges in thermonuclear fusion experiments. The method routinely used for this analysis involves sampling a (usually) rather small set of input signals, such as measurements of magnetic, density and temperature fluctuations, which in most cases are un-evenly sampled in the spatial domain. Appropriate processing of such a set of input data facilitates the detection of the different components in a multi-harmonics spectrum. Furthermore, when the data contains some spatial periodicities, these can be readily used to enhance or eliminate the detection of certain components. A real-time algorithm can then generate a global alarm that is sent to the plant. Under certain specified and pre-determined operational conditions, this may then trigger a feedback control mechanism. For some examples of these activities, the Readers are referred to Chapter3 and Chapter7 and references therein in [13] and Chapter2 and references therein in [14].

One drawback of most of the current MHD detection and control methods is that they can only detect modes when they have become *unstable* (with a growth rate $\gamma_{GROWTH}/\omega>0$, where $\omega>0$ is the mode's angular frequency), i.e. when they may have already had some detrimental effect on the actual plasma operation and performance. On the other hand, an alternative and innovative method is in use on the JET tokamak [15]. This diagnostic technique combines the active excitation (via a set of in-vessel antennas) of magnetic field perturbations which have a very small amplitude at the plasma edge (maximum intensity $|\delta B_{DRIVEN}|<100$mG, i.e. typically $\sim 10^5$ times smaller than the value of the toroidal magnetic field in JET, $B_{TOR}\sim 1$T to $B_{TOR}\sim 4$T) with synchronous real-time detection of the resonant plasma response to such antenna-driven perturbations. This method then allows detecting MHD modes when they are still *stable* (with a damping rate $\gamma_{DAMP}/\omega>0$), i.e. before they could have affected the discharge, which is evidently a much more satisfying situation for plasma control and machine protection.

However, none of the methods described above can be efficiently used for the decomposition of a stable spectrum of MHD modes with the aim to measure their damping rate, because of their mathematical limitations and computational requirements, particularly when real-time, sub-millisecond calculations are needed, and when the measurement spectrum is frequency-degenerate, i.e. it contains multiple temporal components at frequencies which are separated by less than the damping. Conversely, a method based on the *Sparse Representation of Signals*, as implemented in the *SparSpec* code (freeware available at: http://www.ast.obs-mip.fr/article123.html) [16, 17] has

been demonstrated to efficiently and correctly perform the post-pulse [18] and real-time [19, 20] blind and unsupervised signal decomposition of data which are un-evenly sampled in the spatial domain using a (very) small number of measurement points.

Finally, following the successful application of the *Sparse Representation of Signals* to the analysis of actual measurements of different classes of MHD instabilities on the JET tokamak, we have used this method as an "inverse tool" to predict the MHD measurement performance of the ITER array of high-frequency (HF) magnetic probes [21-24]. This has allowed us to comparatively test the measurement performance of different system designs, thus allowing us to propose an optimized diagnostic design [25, 26].

This paper is organised as follows. Starting from existing literature [27], in Section-2 we review the mathematical foundations of the *Sparse Representation of Signals* and of the *SparSpec* code. Section-3 presents some application of this algorithm to the analysis of various MHD instabilities observed on the JET tokamak. Section-4 then deals with the application of a method based on the *Sparse Representation of Signals* to the optimization of the design of the ITER HF magnetic diagnostic system. Finally, Section-5 presents the conclusions of this work and some prospects for future applications to ITER and other complex engineering and scientific systems such as the Square Array Telescope (SKA) [28].

2. SPARSE REPRESENTATIONS OF SIGNALS AND THE *SPARSPEC* CODE.

The A&A problem consists in the analysis of time-series: these can be, for instance, light curves or radial velocity measurements, which are subject to observational constraints, such as day/night alternation and meteorological conditions. The A&A ground-based measurements are therefore always obtained through irregular sampling. An example of such a data set is provided in fig1, showing the observation for the radial velocity curve of the Herbig Ae star HD 104237, obtained over five observing nights of high resolution spectroscopy at the South African Astronomical Observatory during April 1999 [29, 30].

In A&A data analysis (as for MHD analysis in thermonuclear fusion plasmas), the main objective is that of looking for periodicities. For the case of variable stars, and multiple star systems, there are several oscillation modes, some of which are related to the stars' orbits and have to be filtered out when oscillations in other quantities are sought. This leads to the estimation of spectral lines from the data. The irregular sampling can be seen as the application of an irregular Dirac comb w(t) to the original signal y(t) and can be well understood in the Fourier domain:

$$y_s(t) = \begin{cases} \sum_{p=1}^{P} y(t_p)\delta(t-t_p) & \xrightarrow[\text{Transform}]{\text{Fourier}} \quad Y_s(f) = \int_{-\infty}^{\infty} y_s(t) e^{-2j\pi ft} dt = \sum_{p=1}^{P} y(t_p) e^{-2j\pi f t_p} \\ y(t) \times \underbrace{\sum_{p=1}^{P} \delta(t-t_p)}_{w(t)} & \xrightarrow[\text{Transform}]{\text{Fourier}} \quad Y_s(f) = Y(f) \star \underbrace{\sum_{p=1}^{P} e^{-j2\pi f t_p}}_{\mathcal{W}(f)} \end{cases} \tag{1}$$

In eq.(1), $y(t_p)$ are the individual measurements taken at all the time points t_p (for p=1, …, P), from which the irregularly sampled signal $y_s(t)$ is constructed through the filtering via the Dirac delta function $\delta(t-t_p)$, and $Y_s(f)$ is the Fourier Transform (FT) in time of $y_s(t)$. $Y_s(f)$ then corresponds to the convolution of the FT of the original signal Y(f)=FT(y(t)) with the spectral windows W(f), which is the FT of the irregular Dirac comb, W(f)=FT(w(t)).

In the theoretical infinite regular sampling case, the spectral window is the usual Dirac comb and the Fourier transform of the sampled data corresponds to a periodised version of the original signal's FT. This property leads to the well-known Nyquist-Shannon theorem [31] which is not valid in the irregular sampling case. An example of data FT and spectral window is provided in fig2. Hence, the analysis problem becomes that of obtaining a deconvolution of the spectral line data Y(f) from the spectral window W(f). The mathematical modelling for this problem is relatively simple: as the original signal is constituted of a sum of pure frequencies, each data point $y(t_p)$ is expressed as a weighted sum of complex sinusoids, the so-called *atoms*:

$$y\left(t_p\right) = \sum_{l=1}^{L} c_l e^{2i\pi\upsilon_l t_p} + \varepsilon_p \,, \qquad (2(a))$$

where ε_p is the error on the measurement, c_l and υ_l are the complex amplitudes and frequency, and L is the total number of spectral components. The formulation of eq.(2a) presents two problems: first, it is non-linear with respect to the frequencies υ_l, and second, L is unknown a-priori.

The problem described by eq.(2a), which amounts to fitting multiple complex sinusoids to the input data, is a very general signal processing problem which arises in many fields of physics. Such a spectral analysis problem from irregularly sampled data is very common in A&A, where time series acquisition usually suffer from incomplete temporal coverage, in particular periodic gaps caused by the Earth's rotation and revolution, and a-periodic interruptions due to the weather. Many methods have been proposed in the fields of A&A to improve the analysis of such irregularly sampled time series, based on generalizations of the Lomb-Scargle periodogram [2, 3] and Data-Compensated Discrete Fourier Transform [32]. When dealing with data with several frequencies, iterative procedures are generally used [5, 33]. Such methods, however, are inadequate when there are several temporal frequencies and too few measurements. Specific methods have also been developed for short data strings to analyse strictly periodic signals (fundamental frequency ν0 and harmonics frequencies which are an exact multiple of ν_0), such as Phase Dispersion Minimization [34] and string length method [35].

A major simplification [36] of eq.(2a) can be obtained by using a discretization of the frequency axis $f_k=(k/K)*f_{MAX}$, with k=[-K, ..., K], where f_{MAX} is much larger than the largest frequency component that can reasonably be present in the measurements, leading to:

$$y\left(t_p\right) = \sum_{k=-K}^{K} x_k e^{2i\pi f_k t_p} + \varepsilon_p \,, \qquad (2(b))$$

The problem is linear with respect to x_k, but we now must deal with an even larger number of unknown amplitudes x_k and frequencies f_k, as one may take that K>>L to achieve a high resolution analysis. However, the estimation of the spectral lines $\{x_k, f_k\}$ can then now be greatly simplified imposing the *sparsity* of x_k and f_k, i.e. imposing that the x_k and f_k have only a small number of non-zero components. Such a problem can be tackled through the *Sparse Representations* principle. Formally, *Sparse Representations* [17, 37, 38] are representations that account for all information in the input data y(t) with a linear combination of a small number of elementary signals (for instance: sine waves, Diracs, …) called *atoms* that belong to a selected family (a *dictionary*) which contains many such elementary signals. The atoms set is a redundant family, i.e. it does not form a basis as the number of atoms (2K+1, see eq.(2b)) exceeds the dimension P of the signal space, so any signal can be represented by more than one combination of different atoms. Among all these various possible combinations, the one with the smallest number of atoms is the Sparse Representation of the signal. The sparsity of $\{x_k\}$ can be quantified with the L0 (pseudo) norm, i.e. the number of non-zero components in $\{x_k\}$: $\|\mathbf{x}\|_0=\#\{k,|x_k|\neq 0\}$. Hence, the Sparse Representations of $\{x_k\}$ is defined as $\hat{x} = \arg(\min_x \|x\|_0)$, subject to $y = W \bullet x$. Here $\mathbf{y}=[y_1, y_2, \ldots, y_P]^T$ is the vector of data taken at position t_p; $\mathbf{x}=[x_1, x_2, \ldots, x_M]^T$ is the vector of complex amplitudes, and $\mathbf{W}=[\mathbf{w}_{11}, \ldots, \mathbf{w}_{PM}]$ is a matrix where the column vector $\mathbf{w}_k$ corresponds to the k-th atom at the time point t_p for p={1, …, P}. The *Sparse Approximations* of signals [39-41] is the version of the Sparse Representations adapted to noisy data, i.e. $\hat{x} = \arg(\min_x \|x\|_0)$, subject to $\|y = W \bullet x\|_2^2 < \alpha$, where α is a user-defined threshold related to the noise level. Theoretically, the Sparse Approximation problem can also be written as the minimizer of the criterion:

$$J_0(x) = \|\mathbf{y} - W\mathbf{x}\|^2 + \gamma \|\mathbf{x}\|_0, \tag{3}$$

where γ is a penalization parameter related to the noise level. However, to minimize this criterion, one must perform a combinatorial optimization, i.e. sift through all possible combinations of elementary signals, which is intractable for large M. Hence, two kinds of methods have been proposed to get round this problem. The first one, often called a *greedy pursuit* algorithm, iteratively adds atoms to the initial approximation of the signal to improve such approximation [42], which are very similar to iterative procedures used for spectral analysis in A&A [5, 33]. The second one, often called a *convex relaxation* scheme, replaces the L0 (pseudo) norm in eq.(3) with another penalization term, generally based on the L1-norm, such that the criterion may be minimized more easily, particularly when considering optimization of the use of CPU time.

Strictly speaking in fact, the sparsest solution minimizes the least-square criterion penalized with the L0 (pseudo) norm, i.e. the number of non-zero components in the solution. However, minimizing such a criterion requires an exploration of all possible combinations of modes in the input dataset, similarly to the SVD technique proposed in [7], which is very demanding in terms of CPU-time consumption. Such an exploration is in fact avoided in *SparSpec* by considering the

L1-norm, i.e. the sum of the absolute values of the mode amplitudes, instead of the L0 (pseudo) norm penalization.

Here we follow this convex relaxation approach, classically using the L1-norm $\|\mathbf{x}\|_1=\Sigma_k|x_k|$, instead of the L0 (pseudo) norm shown in eq.(3), so that $\hat{x} = \arg(\min_x\|y - \mathrm{W} \bullet x\|_2^2) + \lambda\| y \|_1$. Hence we obtain the criterion:

$$J_1(x) = \left\|\mathbf{y} - W\mathbf{x}\right\|^2 + \lambda\left\|\mathbf{x}\right\|_1 = \left\|\mathbf{y} - W\mathbf{x}\right\|^2 + \lambda \sum_{k=-K}^{K}\left(\left|x_k\right|\right). \quad (4)$$

It can then be easily shown that the criterion of eq.(4) is convex, therefore has no local minima, but, as the number of unknowns may be larger than the number of data points, this criterion is not strictly convex, i.e. the global minimum cannot be a-priori guaranteed to be unique. Moreover, this criterion is not differentiable for $x_k=0$, which is a necessary (but not sufficient) condition for sparsity [43]. In practice, minimizing this L1-norm penalized Least-Square (LS) fitting criterion is much easier than minimizing the original one based on the L0 (pseudo) norm, and many computationally efficient algorithms have been developed, some of which can be made compatible with a real-time system using a 1kHz clock-time. However, minimizing eq.(4) does not necessarily lead to the same solution as minimizing eq.(3), i.e. sufficient conditions for the equivalence between the L0 (pseudo) norm and L1-norm need to be satisfied.

Much theoretical work has been performed to determine the conditions of equivalence between the L0 (pseudo) norm and the L1-norm penalization criteria (see for instance [41, 43, 44]). For example, it can be shown that if the signal can be represented with $\|\mathbf{x}\|<(1+1/\mu)/2$ components, with $\mu=\max_{k\neq l}(|\mathbf{w}_k{}^H\mathbf{w}_l|)$, where $\mathbf{W}^H$ is the Hermitian transposition of **W,** then minimizing eq.(4) will lead to the selection of the same atoms as the solution minimizing eq.(3). Hence, the accuracy of our calculations (both real-time and post-pulse) is also guaranteed by the comparison between a model input spectrum (with/out background noise) and the output spectrum as calculated by *SparSpec* using the actual geometry of magnetic sensors.

Therefore, the choice of the family of atoms is critical in the Sparse Representations (and Approximations) of signals as, with an appropriate choice, these atoms might be well adapted to the signal to be analysed and might lead to a matrix **W** with good analytical and numerical properties. For these reasons, the matrix **W** is often chosen as a family of relatively uncorrelated atoms, such as wavelets, Diracs, pure sine waves, etc …, but cannot be chosen arbitrarily as it is not guaranteed to have the required good properties, as we will show later. For the spectral analysis problem that we analyse here the atoms are driven by the problem itself and therefore we use $w_k=\exp(2i\pi f_k t_p)$, for $p=\{1, \ldots, P\}$. Moreover, the sparsity of the components x_k, hence the L1-norm, has to be computed on the modulus of the complex amplitudes x_k, while the sparse approximation problem is generally studied, only for real-value amplitudes. Finally, note that $|x_k|\neq|\mathrm{Re}(x_k)|+|\mathrm{Im}(x_k)|$, so imposing the sparsity on the complex modulus is radically different in terms of the model than sparsity applied separately on the real and imaginary components [16].

Considering now the particular application of the *Sparse Representation* method to magnetically confined thermonuclear fusion plasmas in a tokamak device, the MHD analysis is based on magnetic and turbulence measurements, and typically starts with an initial Fourier decomposition of the data in the time/frequency domain to obtain the individual frequency components $\psi(\omega)$. As in a tokamak the plasma column has, to a first approximation, 2D boundary conditions along the toroidal direction and on the poloidal plane, perpendicular to the toroidal direction. The spatial structure of the MHD instabilities is determined by further decomposing each frequency component in its toroidal (n) and poloidal (m) harmonics: $\psi(\omega)=e^{-i\omega t}\Sigma_{n,m}A_{mn}e^{in\phi}e^{im\theta}$. Here ϕ and θ are the toroidal and poloidal angle coordinates, respectively, and we have used the fact that in tokamak geometry one single toroidal component with a given n usually has multiple poloidal components due to toroidicity and various other geometrical effects. The aim of mode number analysis is to determine the value of {n, m} of the magnetic instabilities present in the plasma and to estimate their amplitude from data acquired with P detectors un-evenly positioned at angles ϕ_p (θ_p), p={1, …, P} being the suffix labelling the individual sensors used for the measurement.

For generality and consistency with the original A&A notation, in the tokamak plasma fusion problem the Fourier conjugated variables can still be called {*time*, *frequency*}, which can then be the actual toroidal $\{\phi, n\}$ or the poloidal $\{\theta, m\}$ conjugated angle and mode-number variables. This means that the mathematical formulation can be equivalently used for calculating the n- (toroidal) and m- (poloidal) mode numbers by using the relevant sensor geometry. For the determination of the poloidal mode numbers in tokamak geometry, one has to remember that we should consider explicitly the so-called θ_**-correction* [45-47] to the sensors' position, so as to run the mode number decomposition analysis using the correct, i.e. equilibrium-dependent, sensor geometry.

Considering now for simplicity of notation the specific case of toroidal mode number analysis, each measurement $y(t_p)$ can be mathematically modelled with a slight variation of eq.(2a):

$$y\left(\phi_p\right) = \sum_{l=1}^{L} \alpha_l e^{in_l\phi_p} + \varepsilon_p , \tag{5}$$

where n_l and α_l are the unknown mode numbers and amplitudes, respectively, L is the unknown number of modes and ε_p corresponds to the noise on the data for the given p-th sensor, and periodic boundary conditions in ϕ have been used. Thus, the mode detection problem is strictly equivalent mathematically to the A&A spectral analysis problem.

Evaluating the amplitudes α_l and the mode numbers n_l of multiple modes in a multi-harmonic spectrum is a very difficult problem, even if the number of modes in the input spectrum is actually known a-priori. The usual way to tackle this problem is performing a best LS fitting of the input data. However, this criterion has many local minima for real valued spectral peaks [48, 49], hence in principle requiring a combinatorial exploration for integer-valued mode numbers n_l, and an a-posteriori thresholding scheme to differentiate the "correct" from the "wrong" solutions. This is a very CPU-time intensive process and cannot possibly be adapted for real-time applications

on the sub-millisecond time scale required for the analysis of the JET (and ITER) measurements. An alternative solution consists of providing an estimate for the amplitudes of all possible mode numbers in the range {–K, …, K} (where |K| is much larger than the maximum mode number that can be conceivably present in the input spectrum), at the same time enforcing that most of these modes actually have a null amplitude, i.e. a utilizing a *Sparse Approximation*.

The mode detection (i.e. the spectral analysis) problem is particularly difficult in the case of tokamak plasma physics as the data is un-evenly sampled and sparse, because of unavoidable installation constraints on the measurement devices. It can be shown that the difficulty of the spectral analysis problem is closely related to properties of the spectral window, such as the height and positions of its secondary lobes. Indeed, the mathematical problem described by eq.(5) can be expressed equivalently in the Fourier spatial domain as:

$$Y(\nu) = W(\nu) * \sum_{l=1}^{L} \alpha_l \delta(\nu - n_l) + E(\nu) = \sum_{l=1}^{L} \alpha_l W(\nu - n_l) + E(\nu), \qquad (6)$$

where ν is the spatial frequency, $Y(\nu)$ and $E(\nu)$ corresponds to Fourier transform with respect to the angular position ϕ of the data and the noise, δ is the Dirac delta function, the symbol "$*$" is the convolution operator and $W(\nu)$ is the spectral window of the sampling scheme. Thus, if $W(\nu)$ has a high secondary lobe (with an amplitude close to 1) at a frequency ν_0, a mode number n will produce in the Fourier transform $Y(\nu)$ a maximum at $\nu_1=n$ and a secondary maximum at $\nu_2=n\pm\nu_0$, with an amplitude proportional to $W(\nu_2-\nu_1)=W(|\nu_0|)$. This means that it will be difficult to distinguish the actual mode n from the two "aliases" modes at $n\pm\nu_0$, even in the absence of noise in the data. If we consider for simplicity that obtaining the "true" mode number n_0 obeys a normal probability distribution with variance $\sigma^2(n_0)$, i.e. $P_{TRUE}(n=n_0) \mu \exp(-(n-n_0)^2/\sigma^2(n_0))$, then we also find (using a best fit of the data that led to the analysis presented in [25, 26]) that the probability $P_{FALSE}(n=n_0)$ for a *false detection* of n as n_0 due to the secondary lobes in the spectral window when using the *SparSpec* algorithm is $P_{FALSE}(n=n_0) \mu \sigma^2(n_0) \Sigma_i (W(n_i)+W(|n_i|=\nu_0))/W(n_0)$, where the sum is intended on all possible combinations of n_i and ν_0 such that $n_i=n_0\pm\nu_0$.

In thermonuclear tokamak plasmas these lobes are due to regularities in the sampling (for instance when using a spacing larger than the Nyquist condition) and to the low number of sensors. This situation is further compounded by the failure of sensors over time, a problem that cannot easily be rectified due to restricted in-vessel access. As an example, the spectral window for two families of JET high-frequency magnetic sensors is shown in fig3, comparing the data for the original complete set of 11 sensors that could be used in 1997 for toroidal mode number analysis, and for the 7 sensors in that set which can currently (2013) be used for real-time and post-pulse analysis of MHD instabilities. Note that the original dominant $\nu_0=\pm10$ secondary lobe has now been supplemented by an even higher secondary lobe at $\nu_0=\pm4$, which is much more difficult to deal with as the most interesting n-number range is actually within $|n|=1$ and $|n|=10$.

When applied to thermonuclear plasma physics, the problem described by eq.(6) has some

additional requirements with respect to the A&A problem described by eq.(2b), even if its solution can still be obtained using eq.(4). First, the data are complex-valued, implying that the Fourier transform of the data does not satisfy the Hermitian property $\hat{y}(-n) = \hat{y}^*(n)$ as in the spectral analysis of real-valued data. Obviously, the complex-valued data have to be analysed together, conserving the I/Q phase relation between them, and not independently. Second, the mode numbers n_l can only take positive or negative integer values, while in the general spectral analysis problem frequencies take real values. This is a favourable property as the model (2b) works on a discretized frequency grid. For A&A problems, a very fine discretization of the frequency grid is required so that real valued frequencies are not too distant from the nearest frequency on the grid. Note however that a posterior estimation of the out-grid estimation of the detected frequencies can be performed, i.e. using a barycentric estimation of the neighbour frequencies (as we are interested in all the $|x_k|\neq 0$ components and not in the approximation of the signal as $y \sim \Sigma_k w_k x_k$) [16]. Third, in the real time applications we consider for JET (and for ITER), a set of data is acquired every 1ms, therefore the spectral analysis must be completed in an unsupervised manner in the short time between each measurement acquisition.

For the analysis presented here, the atoms are imposed by the model setup in eq.(5) to be pure complex exponential waves, $\mathbf{W}=\{\exp(i n_k \phi_p)\}_{p,k}$, for $p=\{1, \ldots, P\}$ and $k=\{1, \ldots, M\}$, with $n_k=k-K+1$ and $M=2K+1$. Due to the irregular sampling, the atoms are strongly correlated. Indeed, it can be shown that $|\mathbf{w}_k^H \mathbf{w}_l| = W(n_k - n_l)$, so that it corresponds to regular samples of the spectral window. As $W(\nu)$ may take values greater than 1/3 (as shown in fig3), the previous sufficient condition guarantees exact detection only if the signal consists of a single mode number. Nevertheless, it has been shown from many simulations and analysis of measurements using comparisons between different numerical methods that such a solution generally gives very satisfactory results in terms of detection, even in the case of multiple modes [18, 25, 26, 48]. Moreover, for irregular sampling, uniqueness of the global minimizer is almost surely guaranteed if it has less than P/2 non-zero components, where P is the data size [16, 25, 26].

In terms of amplitude estimations, it has been shown [16, 17] that minimizing eq.(4) leads to an under-estimation of the amplitudes of the detected mode numbers due to the L1-norm penalization term. Thus, an a-posteriori LS re-estimation of these amplitudes is usually performed for post-pulse analysis in a second step within the calculations, after the modes have been actually detected. Their amplitudes are computed by minimizing the least square criterion $\|\mathbf{y}-\mathbf{W}_{DET}\mathbf{x}_{DET}\|^2$ where only the non-zero amplitudes of the optimization step are preserved in $\mathbf{x}_{DET}$. Note that this a-posteriori amplitude estimation step is not an absolute necessity for the real-time analysis, as its main objective is to detect the actual modes, their mode numbers and frequency width, and not to precisely estimate their absolute amplitudes, a scaled value being sufficient for this purpose.

Many numerical algorithms are available to minimize criteria such as those of eq.(4) for Sparse Approximations. While for real-valued unknown $\{\mathbf{x}_k\}$ this problem can be written as a classical Quadratic Program, for complex-valued unknown $\{\mathbf{x}_k\}$ it corresponds to a Second-Order Cone

Program [38]. An algorithm based on an iterative Block Coordinate Descent procedure has been previously proposed [16, 17], and implemented in the *SparSpec* code. This procedure consists of performing successive one-dimensional minimization steps with respect to each complex-valued unknown $\mathbf{x}_k$, where each one-dimensional minimization has an explicit solution. This algorithm is very efficient and a correct solution can be typically found in less than 1ms using the rather modest computational resources available to process real-time JET data [19, 20, 27].

A real-time implementation of the proposed modes detection method requires not only an efficient optimization algorithm to minimize eq.(4) but also, and even more importantly for a frequency-degenerate spectrum, an efficient unsupervised tuning of the penalization parameter λ. The penalization parameter λ is related to the noise level [16] and requires an appropriate tuning, since it increases the penalty for those solutions which invoke a larger number of modes. The first order necessary and sufficient optimality conditions for convex non-differentiable functions (often known as the Karush-Kuhn-Tucker optimality conditions [50-52]), provide a physical interpretation for λ: (a) for $\lambda>\lambda_{MAX}=\max_k(|\mathbf{w}_k^H(\mathbf{y}-\mathbf{W}\mathbf{x}_{MIN})|)=\max_k(|\mathbf{Y}(n_k)|)$, the minimizer $\mathbf{x}_{MIN}$ of eq.(4) is identically zero, i.e. the unique solution has no detected modes; (b) for a given λ, the minimizer $\mathbf{x}_{MIN}$ of eq.(4) satisfies $\max_k(|\mathbf{w}_k^H\mathbf{r}|)=\max_k(|\mathbf{R}(n_k)|)<\lambda$, where $\mathbf{r}=\mathbf{y}-\mathbf{W}\mathbf{x}_{MIN}$ is called the residual (data minus the model corresponding to the estimated modes). Hence λ can be interpreted as the maximum peak amplitude allowed in the FT modulus of the residual, and choosing λ to be a fraction $\lambda_{NORM}\in[0, 1]$ of the maximum of the FT of the data $\lambda=\lambda_{NORM}\times\max(|\mathbf{W}^H\mathbf{y}|)$, ensures the FT of the residual $\mathbf{r}$ to be lower up to this fraction relative to the maximum of the data FT. Hence knowledge of the noise level in the measurements helps to determine the optimum value for λ_{NORM} to be used for real-time and post-pulse analysis of MHD fluctuation data.

3. APPLICATIONS OF A *SPARSE REPRESENTATION* METHOD AND OF THE *SPARSPEC* ALGORITHM TO THE ANALYSIS OF MAGNETIC FLUCTUATIONS IN JET TOKAMAK PLASMAS.

The main application of *Sparse Representation* methods and of the *SparSpec* code on JET has been the real-time and post-pulse analysis of Alfvén Eigenmodes [53-56]. Alfvén Eigenmodes (AEs) are a particularly important example of real-time mode detection and tracking in thermonuclear fusion experiments for two essential reasons. First, these waves are a natural Eigenmode of any magnetically confined plasma: their frequency F_{AE} is simply proportional to the ratio between the magnetic field and the square root of the plasma mass:

$$F_{AE} = \left(multiplier\right)\times\frac{B_{TOR}}{4\pi R_{RES}q_{RES}\sqrt{m_p\sum_i n_i A_i}}, \tag{7}$$

and thus represents the balance between the tension force of the ambient magnetic field lines and the plasma inertia. In eq.(7) B_{TOR} is the toroidal magnetic field, n_i and A_i are the density and atomic mass of all ion species, m_p is the proton mass, $q_{RES}(r_{RES})=(2m+1)/2n$ is the value of the safety factor

at the mode resonant position $R_{RES}=R_0+r_{RES}$, where R_0 is the magnetic axis position and r the minor radius. The quantity *multiplier* defines which class of AEs is being investigated: *multiplier*=1 is used for Toroidal AEs (TAEs) and *multiplier*=2 for ellipticity-induced AEs. The analysis of the dispersion relation of AEs can thus provide unique information on the plasma isotopic composition, the safety factor profile and the toroidal rotation frequency via the Doppler shift in the AE mode frequency for different toroidal mode numbers [57-59]. Second, the fusion-born alpha particles (αs) have a supra-thermal speed at birth that is typically well above the Alfvén speed in the usual thermonuclear tokamak plasma conditions. Resonant interaction with AEs is the first wave-particle interaction encountered by the αs during their thermalization process: hence, this mechanism for phase-space and spatial diffusion needs to be appropriately monitored and controlled to guarantee good confinement of the αs themselves s [60, 61].

While in JET the measurements of unstable AEs, i.e. with a negative imaginary component $\gamma<0$ of the mode frequency $\omega=\omega_{AE}+i\gamma$, are obtained using standard high-frequency magnetic diagnostic systems, the measurements of stable AEs, i.e. with a positive $\gamma>0$, are obtained using the so-called Alfvén Eigenmodes Active Diagnostic (AEAD) system [15], as its original (and still currently predominant) aim is indeed that to drive and detect AEs. This diagnostic system works on the principle of active excitation of low-amplitude magnetic perturbations using in-vessel antennas, with maximum driven intensity at the plasma edge $|\delta B_{DRIVEN}|<100$mG, i.e. typically $\sim 10^5$ times smaller than the value of the toroidal magnetic field in JET, $B_{TOR}\sim 1$T to $B_{TOR}\sim 4$T. Active excitation is then combined with synchronous real-time detection of the resonant plasma response to such antenna-driven perturbations, which provides the capability of measuring only the plasma response at the frequency corresponding to the antenna excitation. The AEAD real-time controller, the Alfvén Eigenmodes Local Manager (AELM), constitutes one essential and furthermore worldwide unique component of the JET Real Time Data Network. The measurement of the mode characteristics, such as the frequency, amplitude, toroidal mode number and damping rate, are obtained in real-time through calculations performed on a sub-millisecond time scale by the AELM software. This data is then passed to the Real Time Signal Server [62], which in principle allows implementing a real-time control and feedback system for the modes detected with the AELM by measuring the distance from the marginal stability limit $\gamma/\omega=0$, and calling for a reaction of the plant when the plasma is approaching the limit during the discharge. Further details on the technical implementation of the AELM hardware infrastructure and software can be found in [27].

The *Sparse Representation* method and the *SparSpec* code have been extensively used to obtain results on the dependency of the mode frequency and damping rate for stable AEs on various background plasma parameters, and these results have been presented previously [63-68]. Hence, in this Section we focus our attention to a brief review of the analysis capabilities of the *SparSpec* code and on newer data that may open novel applications of such method on JET (and ITER), specifically in view of the on-going upgrade of the AEAD system [69-71].

The overall accuracy of the *SparSpe*c code for the analysis of post-pulse and real-time data is

evaluated using simulations performed on a synthetic dataset $S_{IN}(\upsilon_n)$:

$$S_{IN}\left(\upsilon_n\right)=\left[\sum_{k=-L_{MAX}}^{k=+L_{MAX}} A_k \exp\left(il_k\upsilon_n+i\delta_k\right)+\sigma_{SIG}\times\left(r_{1k}+ir_{2k}\right)\right]+\sigma_{MEAS}\left(\upsilon_n\right)\times\left(r_{3n}+ir_{4n}\right). \qquad (8)$$

Here $\upsilon_n\in[0, 2\pi]$ is the position of each sensor, and the input signal $S_{IN}(\upsilon_n)$ is constructed as an arbitrary superposition of different components at the integer mode numbers l_k, $k\in[-L_{MAX}, L_{MAX}]$, where L_{MAX} is the highest mode number in the spectrum. Each l_k spectrum component has a fixed or randomized amplitude A_k and relative phase δ_k. The quantities $\sigma_{SIG}\in[0, 1]$ and $\sigma_{MEAS}(\upsilon_n)\in[0, 1]$ represent the standard deviation in the background noise on each spectral component and on the measurement itself at each sensor, respectively, and are known a priori (i.e. they have a fixed and unique value for each simulation) as they can in principle be measured directly on the system when installed. The quantities $\{r_{1k}, r_{2k}, r_{3n}, r_{4n}\}$ are random numbers chosen from a uniform distribution in the interval $[0.0 \rightarrow 1.0]$; note that the random seed used for $\{r_{1k}, r_{2k}\}$ can be different from the one used for $\{r_{3n}, r_{4n}\}$. With this approach, the noise has independent and un-correlated complex components satisfying the circularity property. In general, σ_{SIG} and σ_{MEAS} can be different and, more importantly, σ_{MEAS} can have different values for different sensors. Intuitively, σ_{SIG} can be associated to background noise from the plasma, for instance due to un-coherent turbulence; conversely, σ_{MEAS} is associated with "engineering" errors, such as tolerances on the position and alignment of the sensors, calibration errors, and various effects such as cross-talk, drifts, offset, signal pick-up and bit-noise in the cabling and electronics. These accuracy tests are performed using Matlab R14 on a 2GHz laptop with 1024MB of RAM.

The "confidence level" in the *SparSpec* calculations is then defined by comparing the output results for $\{A_k, l_k\}$ to their input value:

$$\text{confidence level } = \exp\left(-\frac{\left(OutputData-InputData\right)^2}{\left(TotalVarianceInputData\right)^2}\right). \qquad (9)$$

In eq.(9) the total variance on the input data is taken as σ_{TOT} (P being the total number of sensors):

$$TotalVarianceInputData=\sigma_{TOT}$$
$$\sigma_{TOT}=\sqrt{\frac{1}{2L_{MAX}}\sum_{k=-L_{MAX}}^{k=+L_{MAX}}\sigma_{SIG}^2\left|r_{1k}+ir_{2k}\right|^2+\frac{1}{P-1}\sum_{n=1}^{P}\sigma_{MEAS}^2\left(\upsilon_n\right)\left|r_{3n}+ir_{4n}\right|^2}. \qquad (10)$$

This definition of a confidence level is a very stringent criterion to measure whether the scientific requirements for the accuracy of the *SparSpec* code are satisfied. A normal distribution of the output data centred on an expectation value provided by the input data, with the variance taken as the total variance on such data, i.e. precisely as the ones given in eqs.(9, 10), meets the accuracy requirements provided we achieve a confidence level in excess of $e^{-1/4}$=0.7788. This value for the confidence level is obtained when the absolute difference between output and input data is less than half the total variance on the input data.

We have translated this theoretical definition of a confidence level for the analysis of simulated data into the required accuracy for the analysis of actual data by matching the nominal tolerances for the ITER measurement requirements for high-frequency instabilities [22-24], specifically with respect to the accuracy of the toroidal mode number determination. This is very important as, for instance, a nominal 10% or a ±1 tolerance on the toroidal mode number determination leads to very different requirements for the system depending on which "specific" mode number this tolerance is applied to. In terms of physics interpretation and for real-time plasma protection and control applications, wrongly interpreting the n=1 mode as an n=0 or an n=2 mode (i.e. n=n±1) clearly does not have the same implications as wrongly interpreting the n=10 mode as an n=11 or an n=9 mode, i.e. still having a ±1 error on n. Hence, the confidence level defined in eq.(9) corresponds to the ability of obtaining the requested quantity with an accuracy given by the ITER measurement requirements for high-frequency instabilities.

Hence, we have decided to consider that the acceptable error is ±0 on the toroidal mode number and ±15% on the measured mode amplitude $|\delta B_{MEAS}|$ for low-$|n|\leq 5$ modes of importance for plasma protection and control and for real-time measurements. Examples of these modes are the precursor for sawteeth, Edge Localized Modes and disruptions, and radially extended MHD instabilities such as global Alfvén Eigenmodes, Neoclassical Tearing Modes, Resistive Wall Modes and Alfvén Cascades. Conversely, a mode number measurement error ranging from ±1 to ±3 is deemed to be acceptable for MHD instabilities which are only of "physics" interest, for instance core localized Alfvén Eigenmodes with $|n|=6\rightarrow 20$, for which the amplitude $|\delta B_{MEAS}|$ only needs to be measured within ±30%. The required post-pulse measurement accuracies on the mode amplitude and toroidal mode number and can then be summarized as follows:

Figure4 shows the confidence level in achieving the ITER measurement requirements for the evaluation of the toroidal mode number and mode amplitude when applying the *SparSpec* algorithm to a synthetic dataset defined as in eq.(8) using the seven surviving high-frequency magnetic sensors available in 2013 in JET. More technical details on this method can be found in [25, 26]. The result shown in fig4 represent an overall summary of in excess of 50'000 simulation runs, using a frequency-degenerate input mode spectrum that consists of up to 10 (toroidal) modes with the same mode frequency, with randomized relative amplitudes in the range $A_k=0.05\rightarrow 1.00$ and relative phase in the range $\delta_k=0\rightarrow 1.95*\pi$, and input toroidal mode numbers in the range $|n|\leq 30$. The two main *SparSpec* run-time analysis parameters λ_{NORM} and f_{MAX}, where f_{MAX} is the size of the dictionary used in the analysis, were scanned in the range $0.05\leq\lambda_{NORM}\leq 0.95$ and $60\leq|f_{MAX}|\leq 200$, respectively. We note that the confidence level in the *SparSpec* calculations is very high, exceeding the nominal threshold value $=0.7788=e^{-1/4}$, up to at least $|n|=15$, and only drops significantly below this threshold for higher mode numbers $|n|>25$. These very high-$|n|$ modes are of no concern for real-time control applications in JET, and are also of relatively minor interest for JET physics but for in-coherent turbulence studies.

3.1. REAL-TIME AND POST-PULSE MEASUREMENT OF THE TAE MODE FREQUENCY, AMPLITUDE AND DAMPING RATE USING THE SPARSPEC ALGORITHM.

Figure5 shows an overview of the measurement of the damping rate, mode frequency and mode amplitude for TAEs with different toroidal mode numbers. The measurements were obtained in JET using the AEAD system for the He4 discharge #79216, and these results were obtained using the post-pulse implementations of the *SparSpec* algorithm, using λ_{NORM}=0.65 and $|f_{MAX}|$=150. In addition to the TAE data, fig5 also shows some representative plasma background parameters (electron density and temperature, measured with a high-resolution Thomson Scattering diagnostic system; safety factor, obtained combining EFIT [72] reconstruction with MSE and polarimetry measurements), the value of the antenna driving frequency and the value of the central frequency of the n=1 TAE gap computed as in eq.(7) with R_{RES}=3m, q_{RES}=1.5, $\Sigma_i n_i A_i = 4n_{e0}$, and using the real-time and post-pulse measurement of the toroidal magnetic field and of the electron density line-integrated along a chord passing through the plasma centre.

A few points need to be noted for the TAE measurements shown in fig5. The typical uncertainty on the measurement of the mode frequency is within 50Hz, due to the accuracy of the digital synchronous detection used in the AEAD system. For the accuracy on the determination of the mode numbers one has to consider the possible statistical and systematic errors due to the algorithm used to extract such data. For the measurements shown in fig5, the toroidal mode number can be determined exactly (i.e. n=n±0) up to |n|~10, and it is then subject to at least a ±1 or ~10% error for higher-|n| modes. The amplitude of such |n|<10 modes is then known to within a factor ~2, and the damping rate is subject to an uncertainty of the order of 15% for the typical cases that we have considered in this analysis. Finally, fig5 shows that many different toroidal mode numbers are present in the frequency-degenerate spectrum of stable TAEs, and these modes have amplitude and damping rate that can easily vary by up to a factor 10 at any given time point. Hence, an accurate real-time mode number discrimination is clearly an essential ingredient for obtaining damping rate and (at least relative) amplitude data that could meaningfully be used for plasma control purpose. The main differences between the real-time and post-pulse implementation of the *SparSpec* algorithm are described in details in [27] and can be summarized as follows, where we use the labels “RT” and “PP” to indicate the real-time and post-pulse implementations of this algorithm. These differences are essentially due to the CPU and RAM limitations of the real-time analysis, which is performed in JET by the AELM system using a commercial real-time off-the-shelf Emerson Network Power VMEbus 5500 card with a 1GHz PowerPC and 512MB RAM, executing software running under the Wind River VxWorks operating system (i.e. the same software used in the NASA’s Mars rovers, Spirit and Opportunity). The CPU time limit of <850μsec is related to the AELM being a *hard* real-time embedded system: the results of missing a deadline are classed as a failure. For JET operation this results in missing data or a wasted experiment, but avoids the worst case, which would be damage to the AEAD or to the JET machine itself. This is contrary to a *soft* real-time embedded system, which

would simply produce a reduced quality of service, such as a Graphical User Interface suffering sluggish mouse response. Post-pulse processing does not suffer of these limitations in computing power, hence allows for a much greater flexibility and scope in the analysis, but at the expense of a usually much longer computational time.

Figure6 shows the comparison between the real-time and post-pulse measurements of the mode frequency, amplitude and damping rate for some representative toroidal mode numbers for the JET discharge #77417. The post-pulse analysis was performed using λ_{NORM}=0.65 and $|f_{MAX}|$=150, whereas for the real-time analysis we set λ_{NORM}=0.85 and $|f_{MAX}|$=20 to satisfy the CPU and RAM limits. The data were evaluated using the RT and PP implementation of the *SparSpec* algorithm, and for presentation we selected both low-n and high-n modes. We note that the RT and PP measurement of the mode frequency for the different mode numbers shown in fig5 almost exactly overlap, with a difference that is typically less than 100Hz: this is essentially due to the accuracy of the synchronous detection system. Similarly, the damping rate measurement follows almost exactly the same trends in real-time and post-pulse, and the discrepancy in their absolute value is usually well below 15% when the temporal evolution of the mode was well tracked in real-time. On the other hand, the measurement of the absolute value of the mode amplitude is only correct in real-time within a factor 3 to 10, although the trends are sufficiently well reproduced: this is essentially due to the fact that the least-square renormalization of the output amplitudes required by *SparSpec* cannot be implemented in real-time due to the limitations in the available CPU and RAM resources. However, this is an issue that can easily be resolved with a more performing hardware than the one currently used by the AELM system in JET.

In summary, the representative TAE measurements shown in fig5 and fig6 demonstrate that the *SparSpec* algorithm fully satisfies the requirement for accurate mode detection and discrimination not only post-pulse, where in principle "unlimited" computational capabilities are available, but also, and more importantly, in real-time when using very limited computational resources. The next step in JET would be to upgrade the AELM hardware so that even more accurate calculations could be performed in real-time, and then implement a feedback loop where appropriate actuators are activated when the damping rate approaches the marginal stability limit $\gamma/\omega=0$ while the mode amplitude exceeds a certain threshold.

3.2 MEASUREMENT OF THE MODE LOCATION OF UNSTABLE TAES.

The *SparSpec* algorithm can also be used to determine the toroidal and poloidal (m) mode number of unstable TAEs, driven by a population of energetic ions. An example of these measurements is shown in fig7 for the JET discharge #49384, where we want to compare the mode radial location as determined from cross-correlation analysis and from the resonant condition $q_{RES}(r_{RES})=(2m+1)/2n$. For these studies, we compare the post-pulse *SparSpec* toroidal and poloidal mode number results (fig7a) with those obtained using a standard Least Square Fit (LSF) algorithm (fig7b). Whereas with *SparSpec* we obtain multiple components at any given time and frequency point, the LSF algorithm

provides us with what is supposedly the dominant (toroidal, poloidal) mode number. The *SparSpec* analysis was performed using λ_{NORM}=0.65 and $|f_{MAX}|$=150 for the toroidal mode number analysis, and λ_{NORM}=0.35 and $|f_{MAX}|$=300 for the poloidal mode number analysis, respectively. Figure7c shows the mode radial location determined as the Eigenfunction peak using $q_{RES}(r_{RES})=(2m+1)/2n$ and cross-correlation analysis between one magnetic probe located and the plasma edge and ECE and reflectometry measurements viewing various radial positions. Note that to determine the q_{RES} value, we only use the dominant component provided by the *SparSpec* analysis. To first approximation, we find that both the *SparSpec* and LSF algorithms provide an evaluation of r_{RES} which is consistent with the cross-correlation data. However, at a closer inspection we actually see that the trend, indicated by the cross-correlation measurements, of r_{RES} moving towards the magnetic axis as the current profile relaxes and the value of the q-profile drops across the plasma cross-section, is only well reproduced when using the *SparSpec* q_{RES} data. Conversely, the LSF data produce (even if only relatively small) jumps in q_{RES} that are not consistent with the cross-correlation data. The reason for this difference is straightforward: whereas the LSF algorithm effectively forces a best (in the LS sense) fit of the magnetic measurements with one single component, the *SparSpec* algorithm allows multiple components. The dominant one is only selected a-posteriori to obtain q_{RES}, and this turns out to be a more accurate processing method.

3.3 MEASUREMENT OF TURBULENCE SUPPRESSION BY FUSION-BORN ALPHA PARTICLES.

The Deuterium-Tritium Experiment (DTE1) performed in JET in 1997 [73] produced the world record fusion power $P_{FUS}\approx$16MW, with a record fusion energy gain $Q_{DT}\approx$0.65 maintained over about half the plasma energy confinement time τ_E. One of the main purposes of this experiment was that to verify the plasma self-heating by the fusion-born αs: this process requires the as first to thermalize on the electrons, on a time scale $\tau_{\alpha e}$ that is in general comparable with τ_E, and then the electrons are required to heat the ions through energy equi-partition, occurring over a time scale τ_{ei} that is around five to ten times longer than τ_E. This mechanism for the plasma self-heating by the fusion-born αs was fully verified during the DTE1 experiment [74, 75]. However, and totally unexpectedly from a theoretical point of view, at the time of the DTE1 experiment it was also noted that under certain experimental conditions a thermal ion heating was obtained that was much larger than what could be predicted, and furthermore occurring over time scales even shorter than τ_E. This unexpected observation of an anomalous ion heating in the presence of a minority population of fusion-born αs has only been very recently explained in terms of turbulence suppression in the Ion Temperature Gradient (ITG) channel by the αs themselves [76, 77]. This explanation has been obtained by combining methods that have only recently become available, such as the *SparSpec* algorithm for the spectral analysis of the magnetic and turbulence measurements and the GENE code [78] for the numerical simulation of turbulence in the ion and electron channels in the presence of multiple and non-thermal ion species.

Figure8 shows a summary of the spectral measurements of the turbulence in the ion acoustic frequency range, presented as function of the toroidal mode number for three discharges with different densities of αs, and for two phases in the discharge: before and after full thermalization of the αs. These results were obtained using the post-pulse implementation of the *SparSpec* algorithm, with λ_{NORM}=0.15 and $|f_{MAX}|$=500. The very small value of λ_{NORM} and high value of $|f_{MAX}|$ are both needed as the turbulence spectra are incoherent, in principle could extend up to very large toroidal mode numbers (i.e., down to a wavelength smaller than the ion Larmor radius), and have an amplitude which may sit just above the background noise level. Data for negative and positive mode numbers correspond to turbulence in the electron and ion channels, respectively Trapped Electron Modes (TEM) and ITG modes. For the discharge #41069, which does not have αs, the data have been analysed at the same two time points, i.e. before and after full thermalization of the αs, used for the discharges #42847 and #43011, which had αs. Whereas in #41069 the turbulence spectra are very similar at these two time points, in #42847 and #43011 we note a large increase in the TEM turbulence as αs thermalize. More importantly, there is a factor ~2 to ~5 suppression of turbulence in the ITG channel when the αs have not yet thermalized, with the larger reduction occurring in the discharge #42847, which has a larger fraction of αs. Simulations performed with the GENE code indicate that the intensity $|\delta B_{MEAS}|$ and growth rate γ_{ITG} of ITG turbulence in the toroidal mode number range 65<n<120 both decrease as the αs start thermalizing on the background plasma, as indicated by the turbulence measurements. This then allows the core ion temperature T_{i0} to increase on a time scale which is comparable to the energy confinement time τ_E~0.8sec, as measured, but is much faster than the αs slowing-down time on the ions ($\tau_{\alpha i}$~4sec) and the electron-ion energy equi-partition time (τ_{ei}~5sec). Again consistently with the turbulence and ion temperature measurements, the increase in T_{i0} drives an increase in $|\delta B_{MEAS}|$ and γ_{ITG} as the fusion born αs start to fully thermalize, which prevents a further increase in T_{i0} itself.

4. OPTIMIZATION OF THE DESIGN OF THE ITER HF MAGNETIC DIAGNOSTIC SYSTEM.

The ITER HF magnetic diagnostic system is intended to provide measurements of magneto-hydrodynamic (MHD) instabilities with magnitude as low as $|\delta B_{MEAS}|$~10^{-4}G (as measured at the position of the sensors) and up to frequencies >300kHz, with toroidal and poloidal mode numbers up to |n|=30 and |m|=60 [22-24]. Figure9a shows the baseline design for this system as in 2009, built around 2 main arrays for toroidal and 6 main arrays for poloidal mode number detection.

The 2 arrays for toroidal mode number detection are made with 2x18=36 equi-spaced sensors each (indicated by red dots in fig9a) and are positioned at two different heights with respect to the geometrical centre of the machine, using the corners of each equatorial port on the low field side of the vacuum vessel wall. Hence, these two arrays have by construction a 20deg/18-fold periodicity, giving an intrinsic (pseudo-) Nyquist number |n|=18 on each of the two periodic sub-assemblies, whereas the ITER measurement requirements specify accurate detection of modes up to |n|=30.

(We use here the wording pseudo-Nyquist as in fact W(|n|=18)=0.2 and not =1 for a true Nyquist value: this occurs because the two equi-spaced sub-assemblies with 18 sensors each are spatially separated and do not correspond to a single equi-spaced assembly with 36 sensors, which would indeed have W(|n|=18)=1 exactly). This system design has another weakness, namely the absence of sensors for n-number detection on the high field side of the ITER vacuum vessel. This does not allow distinction between ballooning and anti-ballooning instabilities, nor can these arrays be used to diagnose MHD modes during start-up plasmas limited on the high-field side wall.

The poloidal mode number detection system is built around 18 un-evenly spaced sensors located on six (out of the nine) machine sectors, covering the entire poloidal cross-section but for the divertor region. The addition of the in-vessel active ELM coil assemblies to the ITER design would reduce the six m-number arrays to 16 sensors each, as the position of two of the sensors clashes with that of the ELM assemblies. This poloidal mode number detection system uses a large number of sensors, but not optimized: the array redundancy is significant, but the measurement system essentially suffers from a limited number of sensors in each one array.

The toroidal and poloidal mode number detection systems can be improved in the ITER original design layout, with initial provisions already being made for this, by adding a high-resolution mini-array on the horizontal (toroidal analysis) and vertical (poloidal analysis) edges of some of the equatorial ports on the low-field side, as shown in fig9b. For toroidal mode number analysis, the addition of such high-resolution arrays will in principle remove the n=18 toroidal Nyquist value by adding un-evenly spaced sensors to the two baseline periodic sub-assemblies. For poloidal mode number analysis, only one high-resolution array can be added, and this will increase the number of sensors that can be used for such measurements.

Finally, note also that the ensemble of the m-numbers measurement arrays in the six machine sectors give rise to 14x 6-sensors arrays for n-number detection (two of the sensors in the poloidal measurement arrays are in fact located at the corners of the equatorial ports, hence are common with the toroidal measurement arrays). These arrays can in principle be used to detect, and possibly remove, low-n modes up to $|n| \leq 5$ from the measured spectrum, for instance for real-time control and plasma protection applications.

We have performed the baseline analysis and optimization of the ITER HF magnetic diagnostic system using a new approach based on a *Sparse Representation Method*, as implemented in the *SparSpec* algorithm. The *SparSpec* algorithm has been applied to a model dataset of input modes for various implementations of the ITER HF magnetic sensor geometry for n(m)-number detection. The ITER measurement requirements and the expected measurements' errors and tolerances, as highlighted in Table1, are explicitly considered in this algorithm to define the *correct* and the *wrong* detection of the modes.

As the ITER vacuum vessel is still undergoing design changes, a system optimization that takes fully into account in-vessel engineering constraints is not yet possible. Hence, in addition to the physics constraints for the measurement requirements, a *cost function* has been included in the

optimization algorithm to reflect the currently foreseen procurement and installation costs for the sensors. This cost function is constructed as follows:

1) each individual sensors costs 7→10 cost-units end-to-end, i.e. from the initial R&D, to the detailed design and manufacturing, and from installation to the final data acquisition;
2) each high-resolution sensor in any of the equatorial ports bears an additional installation cost of 1→2 cost-units due to the different needs for mechanical fixing, requiring further R&D work and additional mechanical interfaces with the vessel structure;
3) each poloidal sensor located in the regions $60<\theta(\text{deg})<120$ and $270<\theta(\text{deg})<315$ bears an additional installation cost of 1→2 cost-units, due to more difficult cabling access;
4) each high-field side poloidal sensor located in the region $120<\theta(\text{deg})<220$ bears an additional installation cost of 2→3 cost-units, again due an even more difficult cabling access;
5) each high-field side poloidal sensor located in the divertor region $220<\theta(\text{deg})<270$ bears an additional installation cost of 4→7 cost-units, again due to an even more difficult in-vessel cabling access and to need for improved RF screening of image and eddy currents;
6) finally, if we have more than 8 toroidal sensors (including high-resolution ones) in any one of the 9 machine sectors, the cost increases by 1→2 cost-units for each additional group of 8 sensors due to need of installing one further cabling loom in that sector.

The ratio between the confidence level in the measurement performance, and the costs necessary to achieve this performance, as defined above, can then give an additional indication of the overall system performance, one where we have integrated physics and budgetary requirements: the highest ratio defines the cheapest (financially) way to obtain a satisfactory measurement performance.

It is now important to introduce the nomenclature used in the following sub-sections. We use the wording "geometry" to define a specific method to select the number and position of the magnetic sensors. For instance, one "geometry" is made up with 36 un-evenly spaced sensors, and a second geometry still has 36 un-evenly spaced sensors in total, but of these 12 are installed in one high-resolution array in one of the equatorial ports. For each geometry, the actual position of each sensor is selected either ad-hoc (for evenly spaced sensors), or through a pseudo-random algorithm (for un-evenly spaced sensors) that takes into account all potential installation constraints, such as zones where the installation is forbidden (for instance the divertor region in the case of a poloidal array). Because if these installation constraints, the position of each sensor is not truly randomly selected. Hence, each geometry is actually represented by a number of different "sensors' arrangements": for the case of un-evenly spaced sensors, these would correspond to the different (pseudo-) random number realizations used to construct each arrangement of sensors.

The baseline analysis and system optimization is performed by scanning various parameters for the input mode spectrum: number of components with their relative (truly) randomized amplitude, phase and mode number, and standard deviation σ in the background (white) Gaussian noise. The different elements of the cost function described above are then added for each particular sensors'

arrangement, and the overall average is taken as the measure of the cost-normalized measurement performance. Finally, various run-time analysis parameters are in principle required for the *SparSpec* calculations, as described in details in [25-27]. However, only the value of λ_{NORM} and the size (f_{MAX}) of the *SparSpec* dictionary are actually of paramount importance for the simulations reported here: using these previous results, we set λ_{NORM}=0.85 and f_{MAX} to be five times larger than the maximum physical mode number present in the input spectrum.

For the analysis reported here, we considered two main types of geometries, using equi- and un-evenly spaced sensors. In all cases, the position of the sensors takes into account the known engineering and installation constraints, such as those due to ports, gaps between vessel elements, diagnostics, for example. Finally, we can add a high-resolution array to any of the baseline arrays defined above in one (or more) equatorial port(s), as sketched in fig9b. These additional high-resolution arrays can again have equi- or un-evenly spaced sensors. Figure10a and fig10b show some representative example of the test geometries used for this analysis, respectively for the toroidal and poloidal mode number measurement arrays. For comparison purposes, we also show the spectral window W(ν) for the various geometries shown in fig10(a,b), ν being n or m, respectively. The spectral window for all these geometries is well behaved, i.e. it does not show any peaks >0.8 in the mode number range of interest, which would very much complicate the analysis.

Hence, having passed the preliminary test of a well-behaved W(ν), we have then defined four additional and complementary criteria to assess the cost-normalized measurement performance of any given geometry [25, 26]. For each test, we performed 50'000 simulation runs for each of the selected 19 test geometries, most of them being usable for both toroidal and poloidal mode number analysis. Each geometry using un-evenly spaced sensors is represented by at least 10 different sensors' arrangements. Ten of these geometries are labelled as ES# and US# to indicate assemblies with a varying number of evenly (ES) and un-evenly (US) spaced sensors, as follows: #1: no high-resolution sensors; #2; adding 1x5 high-resolution sensors; #3: adding 1x7 high-resolution sensors; #4: adding 1x12 high-resolution sensors; #5: adding 3x5 high-resolution sensors. The BT label (five set-ups) indicates the baseline design for toroidal mode number measurements with 2x18 evenly spaced sensors, and the configurations obtained adding to this baseline assembly [1x5, 1x7, 1x12, 3x5] high-resolution sensors. The BP label (four set-ups) indicates the baseline design for poloidal mode number measurements with 16 un-evenly spaced sensors, and the configurations obtained adding to this baseline assembly [1x5, 1x7, 1x12] high-resolution sensors. The {ES1→ES4} and {US1→US4} geometries can be used for both toroidal and poloidal mode number analysis, as only one equatorial port is required for the high-resolution sensors. Conversely, the ES5 and US5 geometries can only be used for toroidal analysis, as multiple high-resolution arrays are used. For the toroidal analysis, different sensors' arrangements were constructed by changing the equatorial port(s) where the high-resolution array(s) were installed. For poloidal analysis, only the equatorial port can be used, and no HF sensors have been positioned in the divertor region or in the lower-midplane and upper-midplane ports.

The details of the analysis and the results for the four selected tests are shown separately in the following sub-sections. All these analyses have been performed using the same 19 geometries indicated above. We used an input spectrum containing between 3 and 7 modes with known randomly chosen (normalized) amplitudes in the range $0.05 \le A_k \le 1$, relative phases $0 \le \delta_k \le 1.95*\pi$ and random choice of integer mode numbers up to $|n| \le 30$ ($|f_{MAX}|=150$) and $|m| \le 60$ ($|f_{MAX}|=300$) for the toroidal and poloidal mode number analysis, respectively, and scanning the standard deviation in the background noise in the range $0.0 \le \sigma \le 0.3$.

4.1 NOISE TEST ANALYSIS.

For the first test, we consider an input data set made only of white Gaussian noise of known variance, and we determine the 95% and 99% confidence level for not detecting any *true* mode. This allows us to assess if one particular geometry is more prone than the others to mistakenly "recognize" white noise as being a high-n(m) mode. Remembering from fig10a that only the V1 geometry with equi-spaced sensors has W(n)=0 exactly for all mode numbers except n=0 and the pseudo-Nyquist value |n|=18, we immediately realize that this problem is particularly important in ITER, as it is clearly not foreseeable to have a sufficient number of equi-spaced HF magnetic sensors for the spatial Nyquist frequency to exceed the maximum (n, m)-mode that needs to be accurately detected, as equi-spaced toroidal and poloidal arrays would have to have at least 60 and 120 sensors each, respectively. This is unfeasible in terms of in-vessel installation when considering an appropriate system redundancy over the machine's lifetime. Therefore, it becomes paramount to understand if a specific geometry is more prone to *false* mode detection than the others.

A summary overview of this analysis is shown in fig11. We find that the best performing geometry has ~30 un-evenly spaced sensors, but needs around ~40 equi-spaced sensors. For an even higher number of sensors the cost function increases much more rapidly than the confidence level for noise rejection, i.e. the measurement performance of the system becomes much less cost-efficient. We also find that the reduction in the cost-normalized confidence level for noise rejection is much sharper for an equi-spaced geometry as the number of sensors increases above its optimum value. We conclude that geometries made with sub-assemblies with spatial periodicities are inherently more prone to incorrect detection of high-n(m) modes than those using un-evenly distributed sensors. For the baseline toroidal and poloidal designs, the best cost-normalized performance is obtained adding one array of 7 high-resolution sensors to the nominal ITER design, for a total of 43 and 23 sensors, respectively. However in both cases the resulting confidence level values =0.907 (toroidal) and =0.924 (poloidal) are still below the best values =0.935 which is obtained with 25 un-evenly spaced + 1x5 high-resolution sensors.

4.2 FALSE ALARMS ANALYSIS.

For the second test, we consider the statistics of correctly recognizing the given input real modes, to which white Gaussian noise of known variance is added, vs. the occurrence of *false alarms*, i.e.

modes being detected which are not in the input dataset (i.e. detected modes have a different mode number than the input ones) or for which the difference between the input and detected amplitude is larger than the tolerance indicated in Table1 for the corresponding mode number. The geometries giving the higher number of correctly detected modes and the lower values of *false alarms* are then the best choices for actual in-vessel installation.

Figure12 shows a summary of this analysis. We find again that not only the fraction of *false alarms* is lower for the geometries using un-evenly spaced sensors, but it also reaches a local minimum for a lower number of sensors. The addition of one high-resolution array of seven sensors clearly improves the measurement performance of the baseline ITER geometries against detection of false alarms for toroidal and poloidal mode number analysis, at the expense, however, of a larger number of sensors for a higher false alarm fraction.

4.3 RESILIENCE TO THE LOSS OF SENSORS.

For the third test, we consider the resilience in the measurement performance of all the test geometries against the loss of sensors through faults, considering the nominal cases of [10%, 20%, 30%] loss. A measure for this resilience is provided by evaluating the confidence level in achieving the same measurement performance of a sensors' arrangement that has all its sensors when some sensors have been lost: the higher the confidence level over all possible permutations of lost sensors and input spectrum variations, the more resilient is that sensors' arrangement against the loss of sensors. To assess the results of this test, we (logically, but somewhat arbitrarily) choose to define the values =0.85, =0.75 and =0.65 as the thresholds in the confidence level associated to a [10%, 20%, 30%] loss of sensors, respectively, that indicate that a certain geometry still satisfies the measurement performance requirements even when not all sensors are available. Note that the system costs do not enter the evaluation of this particular test, as these costs are defined once and for all when the system is built and do not change if any number of sensors is lost at a later stage during the machine lifetime.

Figure13 shows a summary of this analysis. The threshold values for acceptance of this test are explicitly shown by the horizontal (magenta) lines to guide the eye. Considering the example of a nominal 10% loss of sensors, we find that the nominal ITER geometry for toroidal mode number detection does not satisfy the requirements for the resilience in the measurement performance because of its intrinsic spatial periodicity, and only adding at least one array of 12 high-resolution sensors can correct this problem. For toroidal mode number analysis, an assembly with 25 un-evenly spaced sensors in total, comprising 3x5 high-resolution arrays, satisfies the requirements for resilience in the measurement performance even for a 30% loss of sensors. It is not possible to satisfy the requirements for resilience in the measurement performance against loss of sensors with the nominal ITER geometry for poloidal mode number detection, even when adding up to 12 high-resolution sensors. This is due to the low number of sensors =16 in the nominal design. For poloidal mode number analysis, an assembly with 30 to 35 un-evenly spaced sensors in total,

comprising one array of 12 high-resolution sensors, satisfies the requirements for resilience in the measurement performance even against a nominal 30% loss of sensors.

4.4 TOLERANCE TO INSTALLATION AND CALIBRATION ERRORS AND UNCERTAINTIES.

For the fourth test, we consider two elements, namely that (a) the position of each individual sensor is not absolutely fixed, i.e. as the one given in the installation drawings, but that there is a given volume where that sensor will be located, i.e. as actually installed in-vessel, and (b) there will be uncertainties in the end-to-end calibration of the transfer function for each sensor, causing errors in the determination of the relative amplitude and phase of the signals coming from multiple sensors [47, 79]. To practically understand this last term, consider that the relative phase shift $\Delta\Phi$ between the measurements obtained from two sensors is only due to a calibration error. We can then set $\Delta\Phi=\nu\Delta\varsigma$, where ν is the mode number and ς the corresponding angular coordinate: for any mode number, the "erroneous" relative phase shift corresponds to a "calculated" sensor separation which is not the actual one.

These two elements effectively add an additional free parameter, i.e. a "tolerance" on the nominal position of each sensor as given by an in-vessel survey, which is in principle expected to be accurate to within a few millimetres at worst, i.e. not exceeding an angular tolerance ±0.05deg. However, when considering the usual calibration errors and uncertainties in the equilibrium reconstruction (relevant for poloidal mode number analysis) obtained in current devices, the "calculated" position of each sensor is in fact expected to be correct only to ±1deg at best, and ±3deg for the foreseeable worst case conditions. Given an input spectrum to be detected, we can then "numerically move" the initial location of each sensor within this positional tolerance to achieve the best measurement performance: this artificial displacement will then have no practical consequences for the actual in-vessel installation. Only when the optimization algorithm suggests a larger displacement of the sensors to optimize the measurement performance, we must then change their nominal in-vessel position, which in turns implies that the initial geometry was not optimized.

As the raw magnetic measurements (from which the mode characteristics are obtained) are given by the convolution of the input spectrum with the spectral window, the optimal sensor arrangement is uniquely determined by minimizing the maxima of the spectral window $W(\nu)$ for the required set of integer mode numbers $\{\nu_0\}$, since this reduces the contribution of all "false" modes ν_k to the "true" mode ν_1 due to $W(\nu_k-\nu_1)=W(|\nu_0|)$, for all $\nu_k-\nu_1\in\{\nu_0\}$. Numerically, the test procedure is implemented as follows: we start from an initial sensors' arrangement, and we iterate from this starting point by changing the position of each sensor one at a time by up to ±10deg or until we "hit" the closest nearby sensor. The final optimized arrangement is the one for which the higher amplitudes of the spectral window are reduced to the lowest possible level for the set of integer mode numbers of interest $\{\nu_0\}$ Defining pos_{ITER} as the initial and pos_{OPT} as the final, optimized sensor position, we construct the average shift in the sensor position for a total of NN sensors as:

$$\text{SensorShift} = \frac{1}{NN-1}\sqrt{\sum_{k=1}^{k=NN}\left(pos_{OPT} - pos_{ITER}\right)^2} \quad . \tag{11}$$

We consider that each individual sensors' arrangement satisfies the ITER measurement requirements if the overall average displacement is SensorShift≤2.5deg with a standard deviation std(SensorShift)≤1.5deg (or larger, provided their sum is ≤3.5deg). We then average the results for all arrangements representing one particular geometry. As for the previous test (see Section 4.3), the system costs do not enter this particular analysis, as these costs are defined once and for all when the system is built and do not change due to installation or calibration errors and uncertainties. Figure14 shows a summary of this analysis. For toroidal mode number detection, the baseline ITER geometry satisfies the optimization requirements only when adding at least 1x7 high-resolution sensors. This gives a total of 43 sensors, whereas an assembly with 25 un-evenly spaced sensors in total, comprising 3x5 high-resolution arrays, already satisfies those requirements. The nominal ITER geometry for poloidal mode number analysis does not satisfy the optimization requirements. Conversely, an assembly with 30 un-evenly spaced sensors in total, comprising at least 7 high-resolution sensors, satisfies them.

4.5 OVERALL EVALUATION OF THE MEASUREMENT PERFORMANCE.

Having performed the four tests mentioned above, we can now proceed to an overall evaluation of the measurement performance for the test geometries analysed in this work. To this end, we define a threshold value for each of the individual tests, telling us if such a test has been passed. In that case, we give a value =1 to the (cost-normalized) confidence level in achieving the target measurement requirements. If the test has not been passed, the confidence level is then reduced proportionally to the distance from the set threshold value. The results from the four tests are then averaged: this defines the cost-normalized confidence level in achieving the ITER measurement requirements. The threshold values defining the acceptance of a test as function of the toroidal and poloidal mode numbers for different class of HF instabilities are as follows, using the same units and conventions of the corresponding Sections 4.1 to 4.4, are presented in Table3. For the noise rejection tests, i.e. those presented in Section 4.1, we indicate the fraction of detected modes due to noise. For the false alarms tests, i.e. those presented in Section 4.2, we indicate the fraction of wrongly detected modes. For the tests on the resilience to the loss of sensors, i.e. those presented in Section 4.3, we indicate the confidence level in achieving the same measurement performance of the full measurement array when some sensors are lost. For the positional optimization tests, i.e. those presented in Section 4.4, we indicate the maximum allowed sensor shift and its standard deviation.

Figure15 shows the results of this analysis for some of the test geometries analysed in the previous sub-sections. For clarity, the three cases of [10%, 20%, 30%] loss of sensors are considered separately, and we also separate the analysis for individual (groups of) mode numbers, as in Table3. There are two main reasons for this approach, which are graphically illustrated in fig15.

The ITER measurement requirements for HF instabilities specify four main topics, namely machine protection, basic and advanced control, and physics studies, classified according to the mode numbers. Modes required for machine protection are those with toroidal mode number $|n| \leq 3$ and poloidal mode number $|m| \leq 5$, which correspond to basic instabilities such as precursors for sawteeth, Edge Localized Modes and disruptions, Neoclassical Tearing Modes (NTMs) and Resistive Wall Modes: detection of these modes will call for a hard feedback controlled reaction aimed at protecting the integrity of the machine. Modes required for basic control have similar mode numbers in the range $|n| \leq 5$ and $|m| \leq 10$ and correspond to less dangerous variants of the modes sought for machine protection, so that their detection will call for a softer feedback controlled reaction. Modes required for advanced control usually have $3 \leq |n| \leq 10$ and poloidal mode number $5 \leq |m| \leq 20$, corresponding to Alfvén Cascades and AEs. Finally, modes with higher toroidal and poloidal mode numbers up to $|n| \leq 20$ and $|m| \leq 30$ are classified of interest for dedicated physics studies. Even higher mode numbers are not subject to any detailed measurement specification, and to not enter the assessment of the measurement performance. The classification of these groups of instabilities as function of their mode numbers is somewhat arbitrary and partially overlapping, as for instance global, low m/n=3/2 AEs are usually much more benign modes then m/n=3/2 NTMs, so that the former always falls into the basic control class, whereas the latter may under certain experimental conditions fall into the machine protection class. This is reflected by the (green) vertical lines in fig15, separating the mode numbers into classes: these vertical lines can be "moved" to reflect changing physical understanding and measurement specifications.

Similarly, we somewhat arbitrarily choose to define that an acceptable value for the confidence level in the measurement performance of a given sensors' arrangement is =0.85 when all sensors are still available, and we also set this value to be the same for all classes of HF instabilities, i.e. a flat value independent of the mode number. We then reduce this threshold to again a flat value =0.70 and 0.65 for toroidal and poloidal mode number analysis, respectively, when considering a nominal 30% loss of sensors. This is reflected by the horizontal (magenta) lines in fig15, which can also be "moved" to reflect changing desiderata in the required confidence level. By combining our wishes for the confidence level for the different classes of HF instabilities, we can then determine whether a particular sensors arrangement satisfies the ITER measurement requirements.

Figure15a shows the summary results of this analysis for some representative geometries usable for toroidal mode number detection. We find that only by adding one array of 12 high resolution sensors can we use the baseline 2009 ITER design with 2x18 equi-spaced sensors, but only when all 48 sensors are present: this is simply due to the intrinsic periodicity of the baseline array. However, already a 10% loss makes this modified baseline geometry unable to satisfy the requirements in the measurement performance, unless we install 3x5 high-resolution arrays in well-separated equatorial ports, for instance ports [#3, #10, #14]. This therefore makes a total of >50 sensors in each array used for toroidal mode number detection. When using un-evenly spaced sensors, we can reduce their total number down to 30 if we install 3x5 high-resolution arrays in the same well-separated equatorial

ports. If these ports are too close-by, for instance ports [#8, #9, #10], then we are unable to satisfy the measurement performance requirements with 30% loss of sensors, particularly for higher mode numbers. By installing high-resolution array too close by, we reduce the spatial coverage of the measurements: hence we became very sensitive to which sensors are actually lost through fault. If only one equatorial port is available for HF magnetic measurements, then our best geometry is not as performing and needs at least 35 sensors, including an 1x7 high resolution array, or 40 sensors, if we can only have an 1x5 high resolution array.

Figure15b shows the summary results of this analysis for some representative geometries usable for poloidal mode number detection. We find that not even by adding one array of 12 high resolution sensors can we use the baseline ITER design with 16 un-evenly spaced sensors: this is simply due to the intrinsic low number of sensors in the baseline array. Similar results are obtained when considering two alternative geometries with 32 un-evenly spaced sensors in total, comprising an high-resolution array of 12 and 7 sensors, respectively. Only a geometry with 35 un-evenly spaced sensors in total, comprising one array of 12 high resolution ones, can satisfy the measurement performance requirements for physics studies, i.e. up to $|m| \leq 30$, and this also considering the case of a 30% sensor loss. If we relax this requirement and take into account only modes relevant for advanced control, i.e. up to $|m| \leq 20$, we find two other geometries to be acceptable: the first one still has 35 sensors in total, including one array of 7 high resolution ones, whereas the second requires 45 sensors in total as it only uses one array of 5 high resolution sensors.

In summary, our analysis has demonstrated that the more robust sensor geometry is the un-evenly spaced one, i.e. one without periodicities in the sensors' spacing. For the foreseeable input mode spectra for ITER, a truly un-evenly distributed geometry is the more resilient to the loss of sensors, furthermore being much less sensitive to false alarms caused by background noise in the input spectrum. Conversely, a geometry made up of equi-spaced sub-assemblies has the lowest resilience to the loss of sensors, and the highest sensitivity to false alarms, even if the initial number of sensors is larger than that needed to obtain the required spatial Nyquist number. High-resolution arrays (located in well separated ports for toroidal mode number analysis) are very useful to reduce the total number of sensors required for installation. Finally, our optimization tests indicate that a separation smaller than 2deg to 3deg between adjacent sensors is not necessarily beneficial, even for high-n(m) detection, as random phase shifts due to background noise mask the "true" phase shifts for the closest sensors, which in turns makes it more difficult to detect high-n(m) modes with a sufficiently high confidence level. Keeping in mind the ITER measurement requirement for the HF magnetic diagnostic system, these results mean that it is indeed possible to find an optimum compromise between the need for redundancy, calling for the use of arrays of the largest possible size, the in-vessel installation constraints, which calls for the least possible number of sensors, and the need for having a solution for the n- and m-number analysis which is unique (i.e. irrespective of the number of sensors), robust (i.e. keeping the same accuracy irrespective of the input spectrum) and resilient against the loss of faulty sensors up to a specified value.

SUMMARY, CONCLUSIONS AND AN OUTLOOK TO FUTURE WORK.

We have used recent techniques of signal processing in astronomy and astrophysics, based on the Sparse Representations of Signals, to solve current questions arising in thermonuclear fusion plasmas. Two examples are the detection of magneto-hydrodynamic instabilities, which is now performed routinely in JET in real-time on a sub-millisecond time-scale, and the studies leading to the optimization of the magnetic diagnostic system in ITER. These questions have been solved formulating them as inverse problems, despite the fact that these applicative frameworks are extremely different from the classical use of Sparse Representations, on both the theoretical and computational points of view.

The advantages of using a Sparse Representation method, and particularly algorithms based on the *SparSpec* code, are the high speed at which unsupervised calculations can be performed, coupled with the relative ease with which the results can be understood. As an example, using Matlab R14 on a 2GHz laptop with 1024MB of RAM, the complete post-pulse analysis of the mode number and damping rate data collected during one full JET discharge with the AEAD system takes about 200sec of CPU time when performed using the *SparSpec* algorithm, compared to in excess of 2'000sec of CPU time when performed using an SVD algorithm similar to those presented in [6, 7]. Despite the many hardware limitations of the current AELM system on JET, only with *SparSpec* a similar analysis can be performed in real time on a sub-millisecond time base, as other available algorithms based on SVD methods would clearly exceed the CPU and RAM limits. Whereas it is true that for ITER the real-time hardware resources will be much improved, it will also be clearly beneficial to use them judiciously, i.e. as efficiently and as little as possible.

Similarly, the optimization analysis for the ITER HF magnetic diagnostic system takes advantage of one of the main features of Sparse Representation methods, namely the relative ease with which physics-based tests can be turned without further supervision into precise mathematical properties and specifications for any diagnostic system. Combined with the numerical efficiency of *SparSpec*, and using the methods described in this work, we find that we can fully analyse the cost-normalized measurement performance of one arrangement of magnetic sensors typically within 12 hours of CPU time using Matlab R14 on a 2GHz laptop with 1024MB of RAM.

For forthcoming large engineering and scientific projects, such as ITER and the SKA, it is clear that efficient and unsupervised data analysis, in "real-time" wherever possible, will be of paramount importance. For these projects, "real-time" means that the data analysis will have to be performed over a time scale much faster than those over which the experimental measurements will change, so that a control reaction of some actuators may need to be called upon. Whereas for ITER and perhaps one gigabyte of data for one particular sub-system, real-time means calculations performed on a sub-millisecond time scale, for the SKA collecting hundreds of terabytes of data for one single image the relevant time scale is of the order of a week, i.e. the time it may take to re-deploy some of optics for some of the telescopes to obtain a more accurate image of the same view of the universe. Therefore, the experience with JET data has clearly indicated that, due to their speed, accuracy and

unsupervised operation, Sparse Representation methods are perfectly adapted to achieve the goal of obtaining real-time measurements with an accuracy satisfying the desired requirements in future complex engineering and scientific devices.

ACKNOWLEDGEMENTS.

This work, supported by the European Communities under the contract of Association between EURATOM and CRPP-EPFL, was carried out within the framework of the European Fusion Development Agreement. The views and opinions expressed herein do not necessarily reflect those of the European Commission. This work was also partly supported by the Swiss National Science Foundation. The Authors would like to thank the various members, past and present, of the CRPP, MIT and JET staff that have contributed to the design, installation, commissioning and operation of the Alfvén Eigenmode Active Diagnostic system over more than 10 years of experiments at JET. The Authors would also like to acknowledge the useful discussions we have had during the execution of some of this work with Dr. George Vayakis of the ITER organization.

REFERENCES.

[1]. F. Marvasti, *Non-Uniform Sampling: Theory and Practice*, 2001, Springer-Verlag.

[2]. N.R. Lomb, *Astrophysics and Space Science* **39** (1976), 447.

[3]. J.D. Scargle, *The Astrophysical Journal* **263** (1982), 835.

[4]. D. Roberts, J. Lehar, J. Dreher, *The Astrophysical Journal* **93** (1987), 968.

[5]. G. Foster, *The Astrophysical Journal* **109** (1995), 1889.

[6]. J.S. Kim et al., *Plasma Physics and Controlled Fusion* **41** 1999), 1399.

[7]. M. Hole, L.Appel, *Plasma Physics and Controlled Fusion* **49** (2007), 1971.

[8]. F.M. Poli et al., *Plasma Physics and Controlled Fusion* **50** (2008), 095009.

[9]. E.P. Wigner, *Physical Review* **40** (1932), 749.

[10]. H. Choi, W. Williams, *IEEE Transactions Acoustics Speech Signal Processing Impact Factor* **37** (1989), 86.

[11]. N.E. Huang et al., *Proc. Royal Society London* **A454** (1998), 903.

[12]. S. Zegenhagen, A.Werner et al., *Plasma Physics and Controlled Fusion* **48** (2006), 1333.

[13]. Various Authors, *Progress in the ITER Physics Basis* 2007, *Nuclear Fusion* **47**, 2007.

[14]. E.J. Strait, E.D.Fredrickson, J-M.Moret, M.Takechi, *Fusion Science and Technology* **53** (2008), 304.

[15]. A. Fasoli et al., *Physical Review Letters* **75** (1995), 645.

[16]. S. Bourguignon, H. Carfantan, T. Böhm, *The Astrophysical Journal* **462** (2007), 379.

[17]. S. Bourguignon, H.Carfantan, J. Idier, *IEEE Journal of Selected Topics in Sig. Proc.* **1** (^{2007}), 4.

[18]. A. Klein, H.Carfantan, D.Testa et al., *Plasma Physics and Controlled Fusion* **50** (2008), 125005.

[19]. D. Testa et al., *Fusion Engineering and Design* **86**: (2011), 381.

[20]. D. Testa et al., *Europhysics Letters* **92** (2010), 50001.
[21]. For a general overview of the ITER measurement requirements for the HF magnetic diagnostic system, see Table-2 in the Design Description Document DDD 5.5.A, ITER document reference "N55DDD101-06-12W0.3".
[22]. G. Vayakis et al., *Review of Scientific Instruments* **74** (2003), 2409.
[23]. G. Vayakis et al., *Review of Scientific Instruments* **83** (2012), 10D712.
[24]. A.J.H. Donné et al., *Nuclear Fusion* **47** (2007), S337.
[25]. D. Testa et al. 2010, *Fusion Science and Technology* **57** (2010), 208.
[26]. D. Testa et al. 2010, *Fusion Science and Technology* **57** (2010), 238.
[27]. D. Testa, H.Carfantan, A.Goodyear, *Implementation of a novel real-time controller for the detection and tracking of magneto-hydrodynamic instabilities on the JET tokamak*, accepted for publication in Plasma and Fusion Research, September 2013.
[28]. see SKA website http://www.skatelescope.org/ and arXiv:astro-ph/0409274.
[29]. Böhm, C. Catala, L. Balona, B. Carter, *Astronomy & Astrophysics* **427** (2004), 907.
[30]. A. Fumel, T.Böhm, *Astronomy & Astrophysics* **540** (2012), A108.
[31]. C.E. Shannon, *Communication in the presence of noise*, Proc. Institute of Radio Engineers **37** (1949), 10; reprinted in: *Proc. IEEE* **86** (1998), 447.
[32]. J. Lafler, T.D. Kinman, *The Astrophysical Journal Suppliment* **11** (1965), 216.
[33]. D.F. Gray, K. Desikachary, *The Astrophysical Journal* **181** (1973), 523.
[34]. M.M. Dworetsky, *Monthly Notices of the Royal Astronomical Society* **203** (1983), 917.
[35]. P. Stoica, R.L. Moses, B. Friedlander, T. Söderström, *IEEE Transactions Acoustics Speech Signal Processing Impact Factor* **37** (1989), 378.
[36]. M.D. Sacchi, T.J.Ulrych, C.Walker, *IEEE Transactions Acoustics Speech Signal Processing Impact Factor* **46** (1998), 31.
[37]. D.L. Donoho, *Jour. Comm. on Pure & Applied Math*. **59** (2006), 797.
[38]. D.M. Malioutov, *A sparse signal reconstruction perspective for source localization with sensor arrays*, Master Thesis (2003), MIT.
[39]. S.S. Chen, D.L. Donoho, M.A. Saunders, *SIAM Journal on Scient. Comp*. **20** (1998), 33.
[40]. J-J. Fuchs, *IEEE Transactions on Information Theory* **50** (2004), 1341.
[41]. J.A. Tropp, *IEEE Transactions on Information Theory* **52** (2006), 1030.
[42]. J.A. Tropp, *IEEE Transactions on Information Theory* **50** (2004), 2231.
[43]. P. Moulin, J. Liu, *IEEE Transactions on Information Theory* **45** (1999), 909.
[44]. J-J. Fuchs, *IEEE Transactions on Information Theory* **51** (2005), 3601.
[45]. V. Merezhkin, *Soviet JETP* **4** (1978), 152.
[46]. O. Kluber et al., *Nuclear Fusion* **31** (1991), 907.
[47]. D. Testa, A. Fasoli, E. Solano, *Review of Scientific Instruments* **74**, (2003), 1694.
[48]. D.L. Donoho, M. Elad, V.N. Temlyakov, *IEEE Transactions on Information Theory* **52** (2006), 6.

[49]. J.A. Tropp, *IEEE Transactions on Information Theory* **52** (2006), 1030.
[50]. H.W. Kuhn, A.W.Tucker, *Nonlinear Programming*, Proceedings of 2nd Berkeley Symposium (Berkeley: University of California Press, 1951), 481.
[51]. W. Karush, *Minima of Functions of Several Variables with Inequalities as Side Constraints*, M.Sc. Dissertation (1939), Dept. of Mathematics, Univ. of Chicago, Chicago (USA).
[52]. D.P. Bertsekas, *Nonlinear Programming* (2nd edition: 1999), Athena Scientific (Belmont, USA).
[53]. C.Z. Cheng, L. Chen, M.S. Chance, *Annals of Physics* **161** (1985), 21.
[54]. R. Betti, J.P. Freidberg, *Physics of Fluids B* **3** (1991), 1865.
[55]. M.S. Chu et al., *Physics of Fluids B* **4** (1992), 3713.
[56]. A.D. Turnbull et al., *Physics of Fluids B* **5** (1993), 2546.
[57]. A. Fasoli et al., *Physics of Plasmas* **7** (2000), 1816.
[58]. S. Sharapov et al., *Physics Letters A* **28** (2001), 127.
[59]. A. Fasoli et al., *Plasma Physics and Controlled Fusion* **44** (2002), 159.
[60]. W.W. Heidbrink, *Physics of Plasmas* **9** (2002), 2113.
[61]. G. Vlad, S.Briguglio, G.Fogaccia, F.Zonca, *Nuclear Fusion* **46** (2006), 1.
[62]. Q.A. King, H.Brelen, *An Experimental Control Facility at JET*, JET-P(98)24 (1998), Joint European Torus, Abingdon (UK) (weblink: http://www.iop.org/Jet/fulltext/JETP98024.pdf).
[63]. D. Testa et al., *Nuclear Fusion* **50** (2010), 084010.
[64]. D. Testa, D. Spong, T. Panis, P.Blanchard, A.Fasoli, *Nuclear Fusion* **51** (2011), 043009.
[65]. T. Panis, A. Fasoli, D. Testa, *Nuclear Fusion* **52** (2012), 023013.
[66]. T. Panis, A. Fasoli, D. Testa, *Nuclear Fusion* **52** (2012), 023014.
[67]. D. Testa, T. Panis, P. Blanchard, A. Fasoli, *Nuclear Fusion* **52** (2012), 094006.
[68]. D. Testa, P. Blanchard, T. Panis, *On the Measurement of the Radial Profile of the Plasma Isotopic Composition Using Alfvén Eigenmodes*, submitted to Nuclear Fusion Letters, September 2013.
[69]. P. Woskov et al., *New Digital Control System for the JET Alfvén Eigenmode Active Spectroscopy Diagnostic*, GP8.00129, Proceedings 54th Annual Meeting of the APS Division of Plasma Physics, October 29th –November 2nd 2012, Providence (USA).
[70]. T. Debelle et al., *Toroidal Alfvén Eigenmode Amplifier Control at JET Using Commercial FPGA and PXI Platform to Study Plasma Instabilities*, 11th International Symposium on Fusion Nuclear Technology (ISFNT), 16-20 September 2013, Barcelona (Spain).
[71]. A. Fasoli, P. Blanchard, D. Testa, *New capabilities of the JET Alfvén Eigenmode antenna system*, ITPA Topical Group Meeting on Energetic Particles, Culham (UK), 22-25 April 2013.
[72]. L. Lao, H. St.John, R.D. Stambaugh, A.G. Kellman, W. Pfeiffer. *Nuclear Fusion* **25** (1985), 1611.
[73]. M. Keilhacker for the JET team, *Nuclear Fusion* **39** (1999), 209.
[74]. P.R. Thomas et al., *Physical Review Letters* **80** (1998), 5548.

[75]. P.R.Thomas for the JET team, *Nuclear Fusion* **39**(1999), 1619.
[76]. D.Testa, M.Albergante, *Europhysics Letters* **97** (2012), 35003.
[77]. D.Testa, M.Albergante, *Nuclear Fusion* **52** (2012), 083010.
[78]. F.Jenko et al., *Physics of Plasmas* **7** (2000), 1904.
[79]. R.F. Heeter, A.Fasoli, S.Ali-Arshad, J-M.Moret, *Review of Scientific Instruments***71** (2000), 4092.

toroidal mode number	**acceptable error on toroidal mode number**	**acceptable error on mode amplitude**
$\|n\|\leq 5$	error=0 ➔ CORRECT error≠0 ➔ WRONG	error≤15% ➔ CORRECT error≥15% ➔ WRONG
$\|n\|>5$	$\|error\|\leq \min(\|n\|/10, 3)$ ➔ CORRECT $\|error\|\geq \min(\|n\|/10, 3)$ ➔ WRONG	error≤30% ➔ CORRECT error≥30% ➔ WRONG

Table 1: The measurement requirements on the toroidal mode number and mode amplitude which are used to define correct and wrong mode detection with the SparSpec algorithm.

	SparSpec-RT	**SparSpec-PP**
calibration	fixed value at 200kHz	full frequency-dependence
input data	up to 8 complex–valued signals from magnetic measurements only one normalization signal for the antenna drive	up to 16 complex–valued signals from magnetic and turbulence measurements selection between many normalization signals for the antenna drive
output data	many amplitude and phase pairs, one pair for each selected mode number	many amplitude and phase pairs, one pair for each selected mode number
algorithm	least-square renormalization of output amplitude not implemented	least-square renormalization of output amplitude implemented
CPU limit	850μsec @1GHz	un-limited (user choice of hardware)
RAM limit	512MB	un-limited (user choice of hardware)
maximum |n|	$\|n\|\leq\|f_{MAX}\|=15$: mode number determined in real-time with relative error $\|\Delta n/n\|\leq 0.1$	$\|n\|\leq\|f_{MAX}\|=30$: mode number determined post-pulse with relative error $\|\Delta n/n\|\sim 0.1$

Table 2: Comparison and differences between the real-time and post-pulse implementation of the SparSpec algorithm.

	Machine Protection	Basic Control	Advanced Control	Physics Studies
Mode Numbers	n|≤3, |m|≤5	n|≤5, |m|≤10	3≤|n|≤10, 5≤|m|≤20	10≤|n|≤20, 20≤|m|≤30
Noise Rejection	0%	0%	10%	30%
False Alarms	0%	0%	10%	30%
Sensor Loss: 10%	95%	95%	85%	70%
Sensor Loss: 20%	90%	90%	75%	60%
Sensor Loss: 30%	85%	85%	65%	50%
Sensor Shift	(1.5±0.5)deg	(1.5±0.5)deg	(2.0±1.0)deg	(2.5±1.5)deg

Table 3: The threshold values used to define acceptance of the tests described in Section 4.1 to 4.4, for the different classes of HF instabilities in the corresponding mode number range.

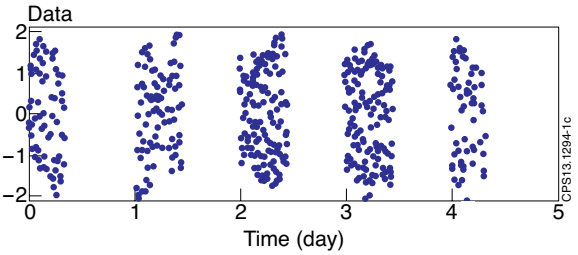

Figure 1: (reproduced from [27]). Observation for the radial velocity curve of the Herbig Ae star HD 104237. These data correspond to five observing nights of high resolution spectroscopy at SAAO (South African Astronomical Observatory) during April 1999. The irregular data sampling due to day/night alternation is very clear.

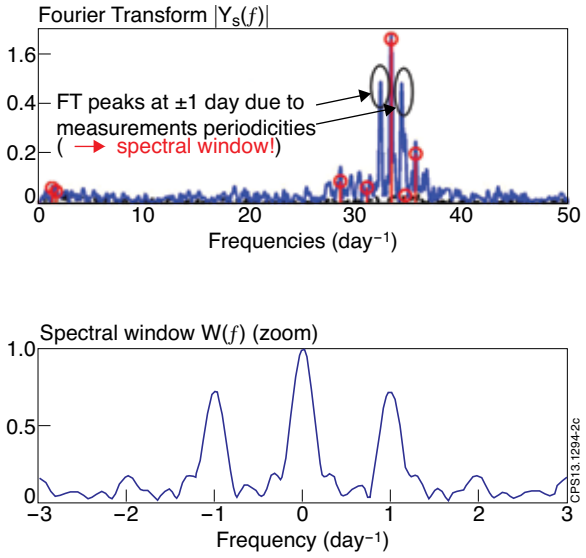

Figure 2: (reproduced from [27]). Top frame: Fourier Transform of the data (blue line) presented in fig1 and SparSpec detection results. Various peaks have been detected (indicated by the red vertical lines terminating in a red circle), the lower frequency ones being related to various orbital movements residuals. The black dotted line corresponds to the FT of the estimation residuals. Bottom frame: the (zoomed) spectral window for the measurements presented in fig1: there are very clear ±1 secondary lobes corresponding to the one-day periodicity in the lack of measurements. The sidebands peaks at ±1 day are therefore removed from the FT data in the detection results shown in the top frame.

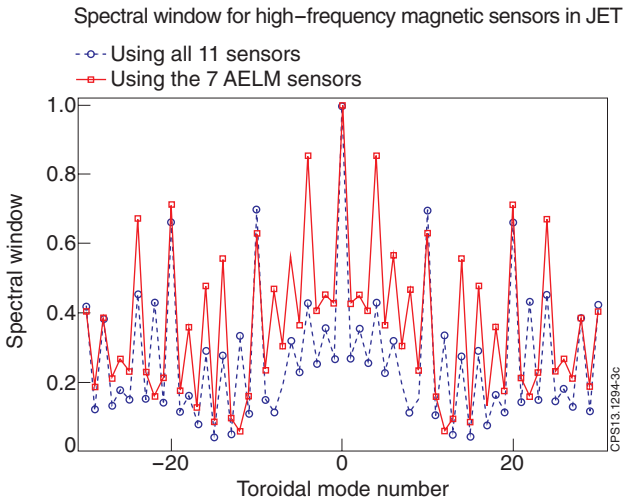

Figure 3: (reproduced and adapted from [27]). The spectral windows W(ν) for the original (1997) and complete set of 11 high-frequency magnetic sensors of JET usable for toroidal mode number analysis, and for the seven surviving sensors between them that can currently (2013) be used. Note that the original secondary lobe at n=±10 with W(ν)=0.70 has now been supplemented by an even higher secondary lobe at n=±4 with W(ν)=0.87, which is much more difficult to deal with.

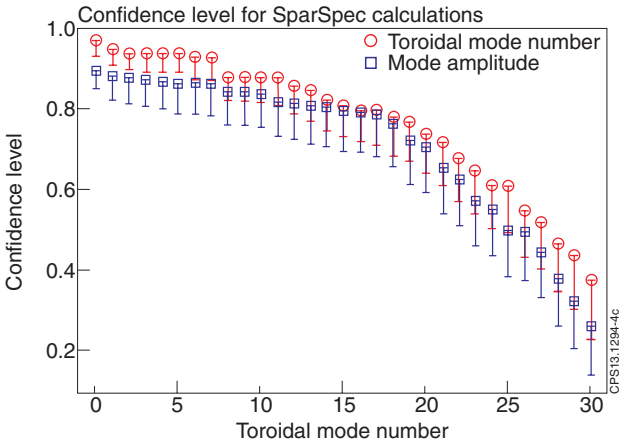

Figure 4:The confidence level in achieving the ITER measurement requirements for the evaluation of the toroidal mode number and mode amplitude when applying the SparSpec algorithm to a synthetic dataset defined as in eq.(8) using the seven surviving high-frequency magnetic sensors available in 2013 in JET. The simulation results are symmetric with respect to the toroidal mode number within the simulation accuracy, hence only the positive-n half spectrum is plotted. The confidence level is very high, exceeding the threshold value $=0.7788=e^{-1/4}$, up to at least $|n|=15$, and only drops significantly for higher mode numbers $|n|>25$. In excess of 50'000 simulation runs were performed to produce this graph, using a frequency-degenerate input mode spectrum that consists of up to 10 modes, with randomized relative amplitudes $A_k=0.05\rightarrow1.00$, relative phase $\delta_k=0\rightarrow1.95*\pi$ and input toroidal mode numbers up to $|n|\leq30$. The two main SparSpec run-time analysis parameters λ_{NORM} and f_{MAX} were scanned in the range $0.05\leq\lambda_{NORM}\leq0.95$ and $60\leq|f_{MAX}|\leq200$, respectively

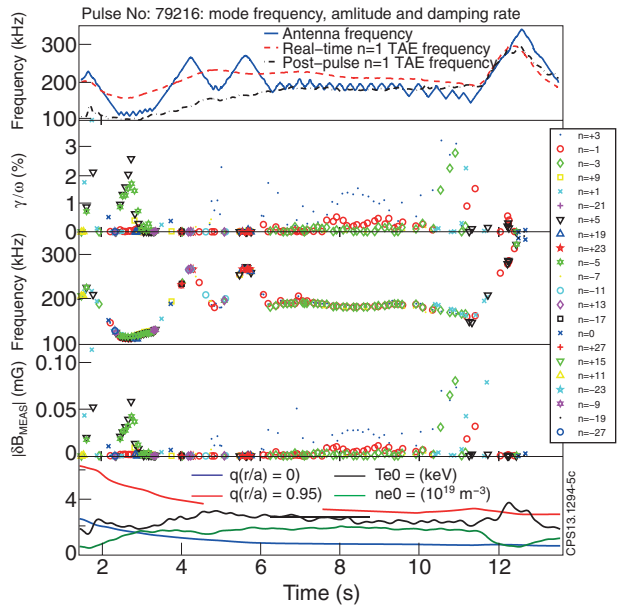

Figure 5: Measurement of the mode damping rate (frame-b), mode frequency (frame-c), and mode amplitude (frame-d) for TAEs with different toroidal mode numbers for the He4 discharge #79216. These results were obtained using the post-pulse implementations of the SparSpec algorithm, using $\lambda_{NORM}=0.65$ and $|f_{MAX}|=150$. The main plasma parameters are shown in frame-e: q(r/a) is the value of the q-profile at different normalized radial positions r/a (where a is the plasma minor radius), T_{e0} and n_{e0} are the electron temperature and electron density on the magnetic axis (at r/a=0). Frame-a show the antenna driving frequency, and the value of the central frequency of the n=1 TAE gap as computed using the real-time and the post-pulse data.

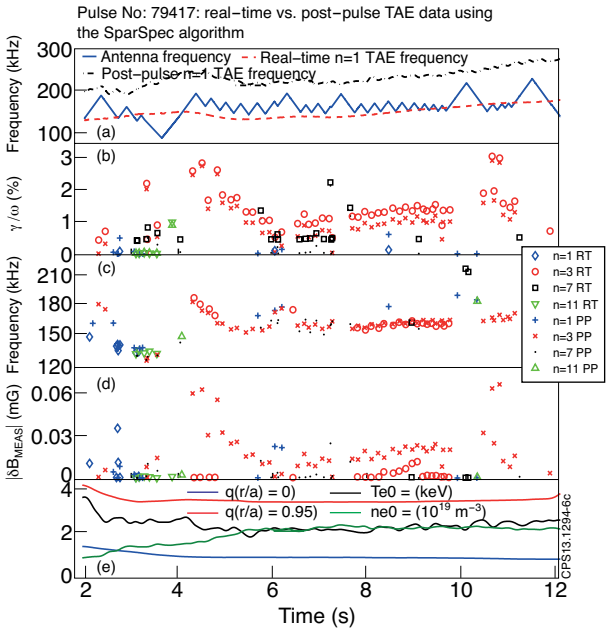

Figure 6: Comparison between the real-time and post-pulse measurement of the mode damping rate (frame-b), mode frequency (frame-c), and mode amplitude (frame-d) for TAEs with different toroidal mode numbers for the D2 discharge #77417. The post-pulse analysis was performed using λ_{NORM}=0.65 and $|f_{MAX}|$=150, whereas for the real-time analysis we set λ_{NORM}=0.85 and $|f_{MAX}|$=20 to satisfy the CPU and RAM limits. The antenna driving frequency, the value of the central frequency of the n=1 TAE gap as computed using the real-time and the post-pulse data and the main plasma parameters are shown in frame-a and frame-e, respectively, using the same format of fig5.

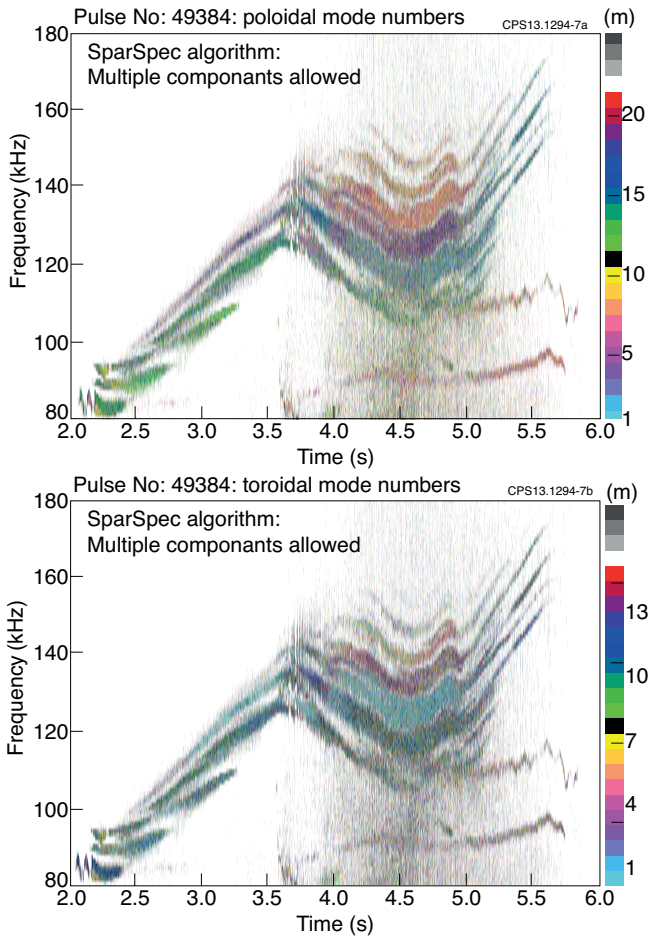

Figure 7a: Measurement of the toroidal (top frame) and poloidal (bottom frame) mode numbers for unstable TAEs driven by an energetic ion population. The toroidal mode numbers are measured using magnetic probes located on the low-field-side wall, whereas for the poloidal mode number analysis we combine low- and high-field side probes and use the so-called θ correction [45-47] to the probes' position to map the probe geometrical location on the vessel wall onto the corresponding one on the resonant flux surface given by r_{RES}. Here the analysis is performed using the post-pulse implementation of the SparSpec algorithm, allowing for multiple components at any given time and frequency point, setting λ_{NORM}=0.65 and |fMAX|=150 for the toroidal mode number analysis, and λ_{NORM}=0.35 and $|f_{MAX}|$=300 for the poloidal mode number analysis, respectively.*

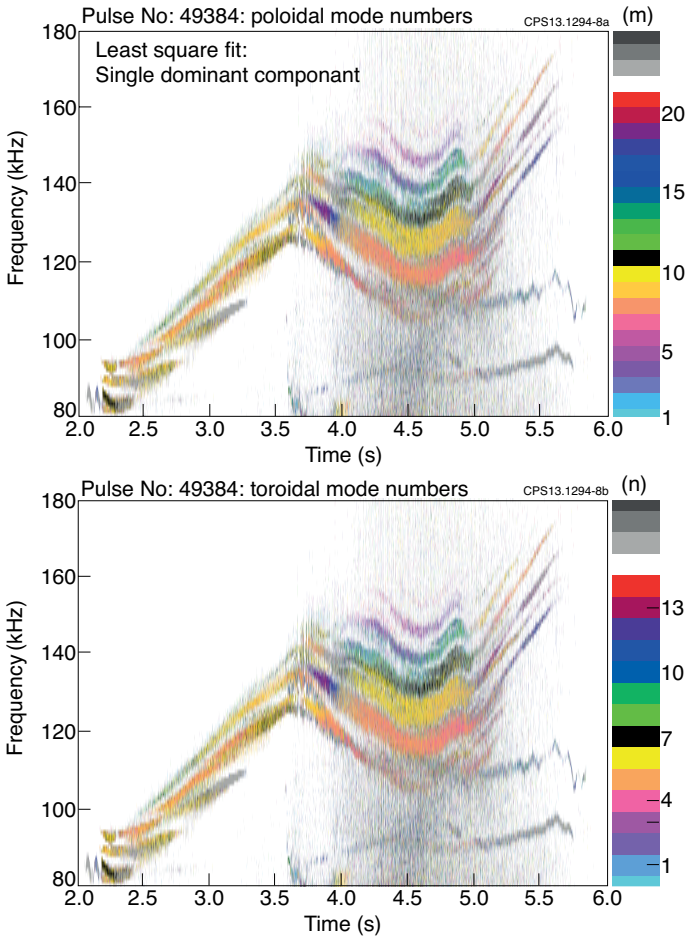

Figure 7b: The same data and plotting conventions of fig7a, but here the analysis is performed using a standard Least Square Fit (LSF) algorithm, which effectively forces the detection of the one single "dominant" component that best fits the data in a LS sense.

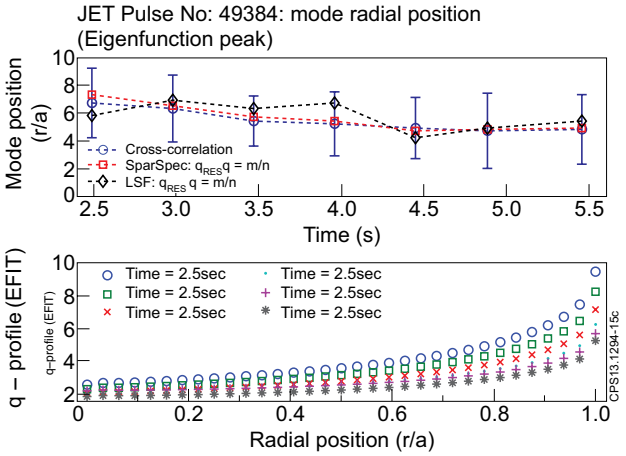

Figure 7c: Comparison of the mode radial position, defined as the peak in the radial Eigenfunction, obtained through cross-correlation analysis and using $q_{RES}(r_{RES})=(2m+1)/2n$, with the toroidal and poloidal mode numbers provided by the SparSpec and LSF algorithms. The vertical "error bar" for the cross-correlation data indicates the estimated width of the radial mode Eigenfunction. We also show the EFIT reconstruction of the q-profile. The three estimates of rRES are broadly consistent with each other, but we note that as the current profile relaxes and the q-value drops across the entire plasma cross-section, the cross-correlation analysis shows that the mode radial location progressively and smoothly shifts inwards towards the magnetic axis, and this trend is only captured correctly when using the SparSpec data to obtain r_{RES}.

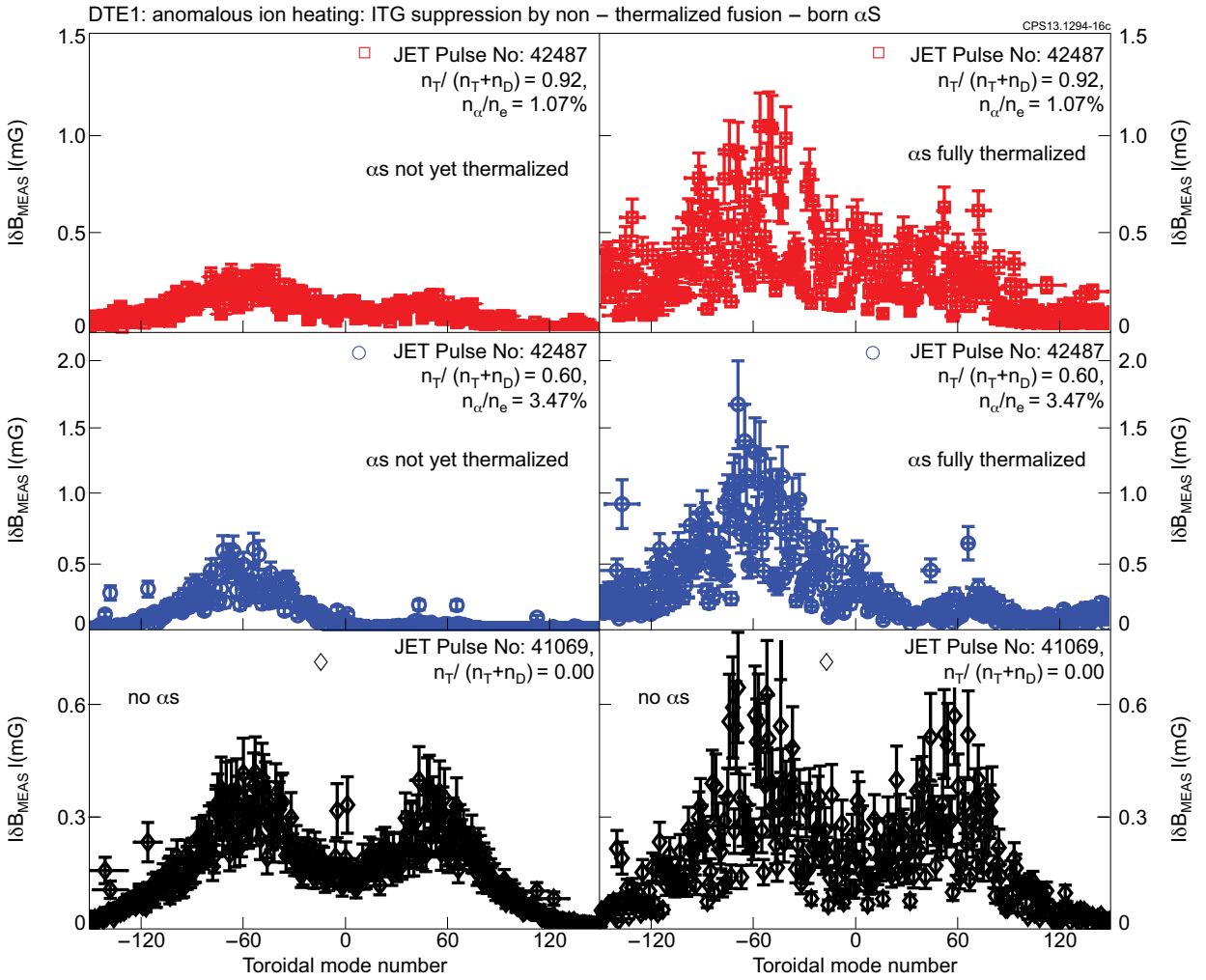

Figure 8: Summary of the turbulence spectral data for the alpha heating experiment during the JET DTE1 campaign. The data are shown as function of the toroidal mode number for three discharges with different densities of α particles. The data are shown separately for two phases in the discharge: before and after full thermalization of the αs. These results were obtained using the post-pulse implementation of the SparSpec algorithm, with λ_{NORM}=0.15 and $|f_{MAX}|$=500.

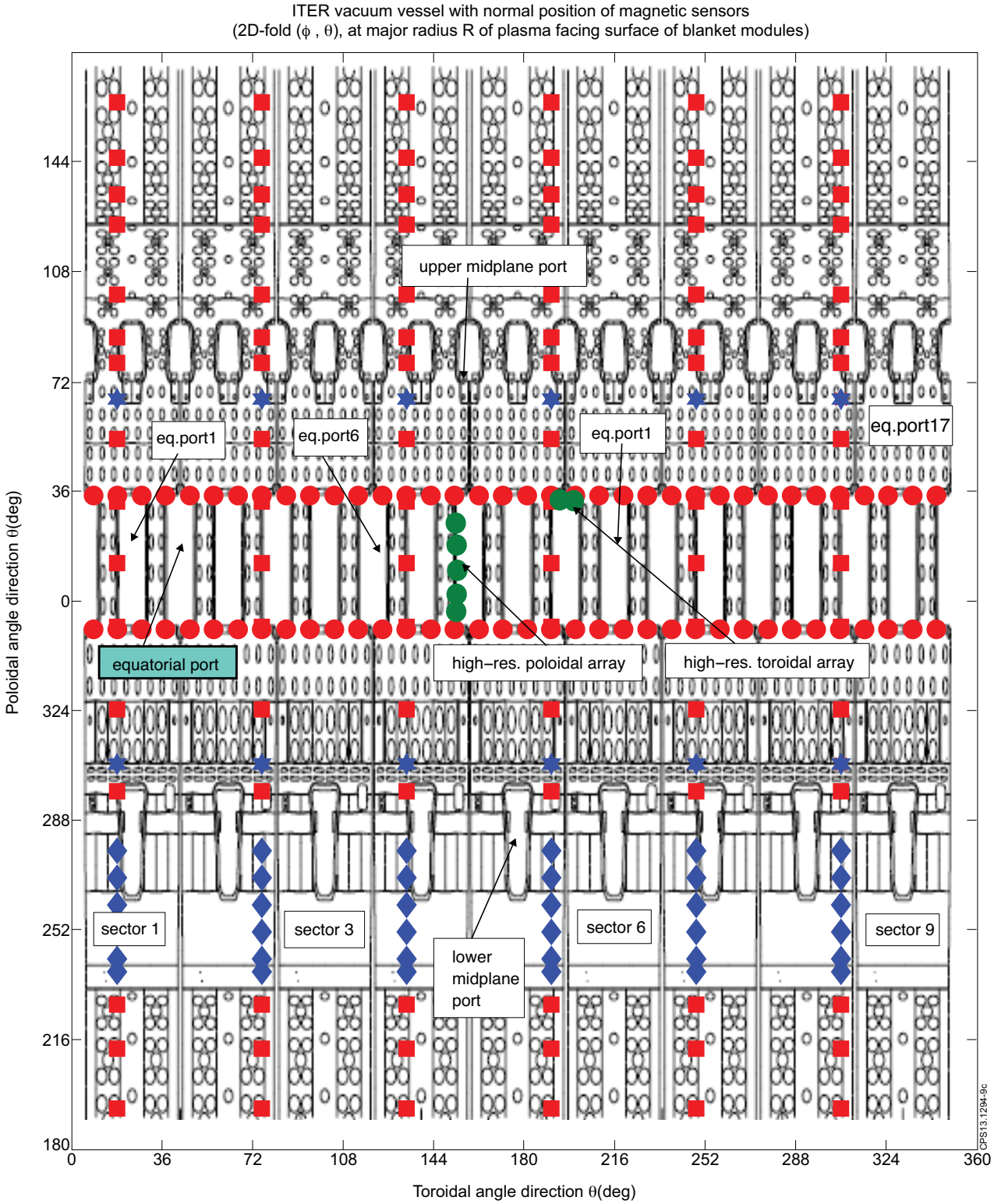

Figure 9a: The proposed layout for the ITER HF magnetic diagnostic system as in 2009, for toroidal (filled red circles) and poloidal (filled red square) mode number; the filled blue lozenges indicate the HF magnetic sensors in the divertor region, blacked-out in this analysis as the presence of the divertor and shaping coils induces parasitic and eddy currents in the surrounding metal structures that prevent reliable measurements of HF instabilities using magnetic pick-up sensors; the filled blue stars indicate the sensors that have been removed because their position clashes with that of the newly designed active coils for ELM control.

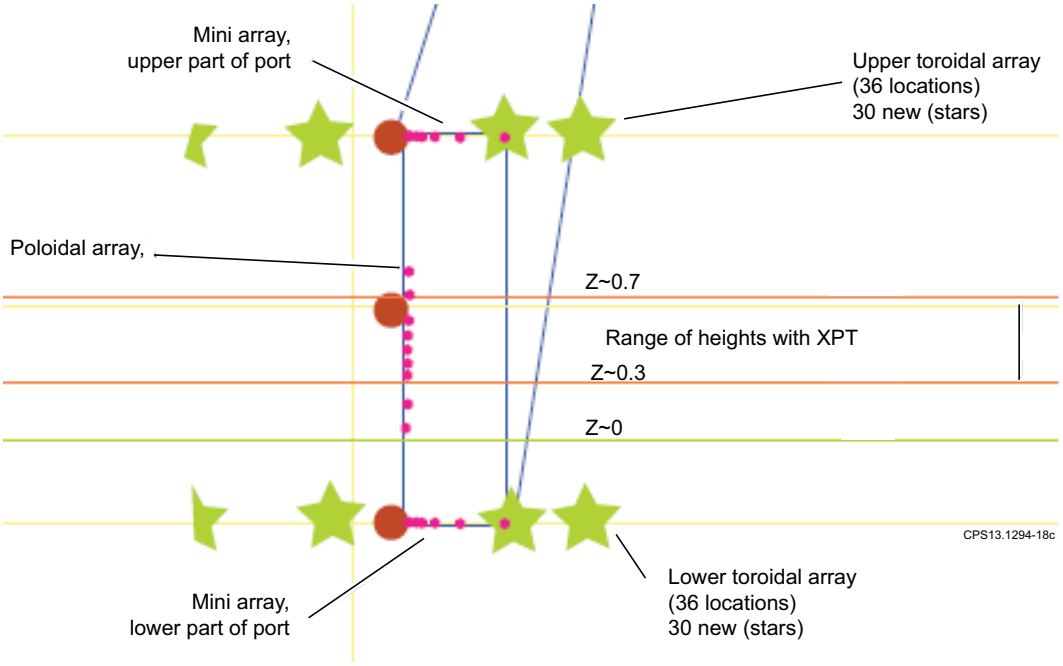

Figure 9b: The proposed implementation for the high-resolution toroidal and poloidal arrays (small red dots) to be located on the horizontal and vertical edges of some of the equatorial ports. The poloidal mode number measurement arrays are located in sector number: [1, 3, 4, 6, 7, 9], whereas the poloidal mode number measurement arrays are only located on the low-field side at the Z-height of the horizontal edges of the equatorial ports; with the green stars, an indicative layout for the high-resolution arrays that can be installed in these equatorial ports.

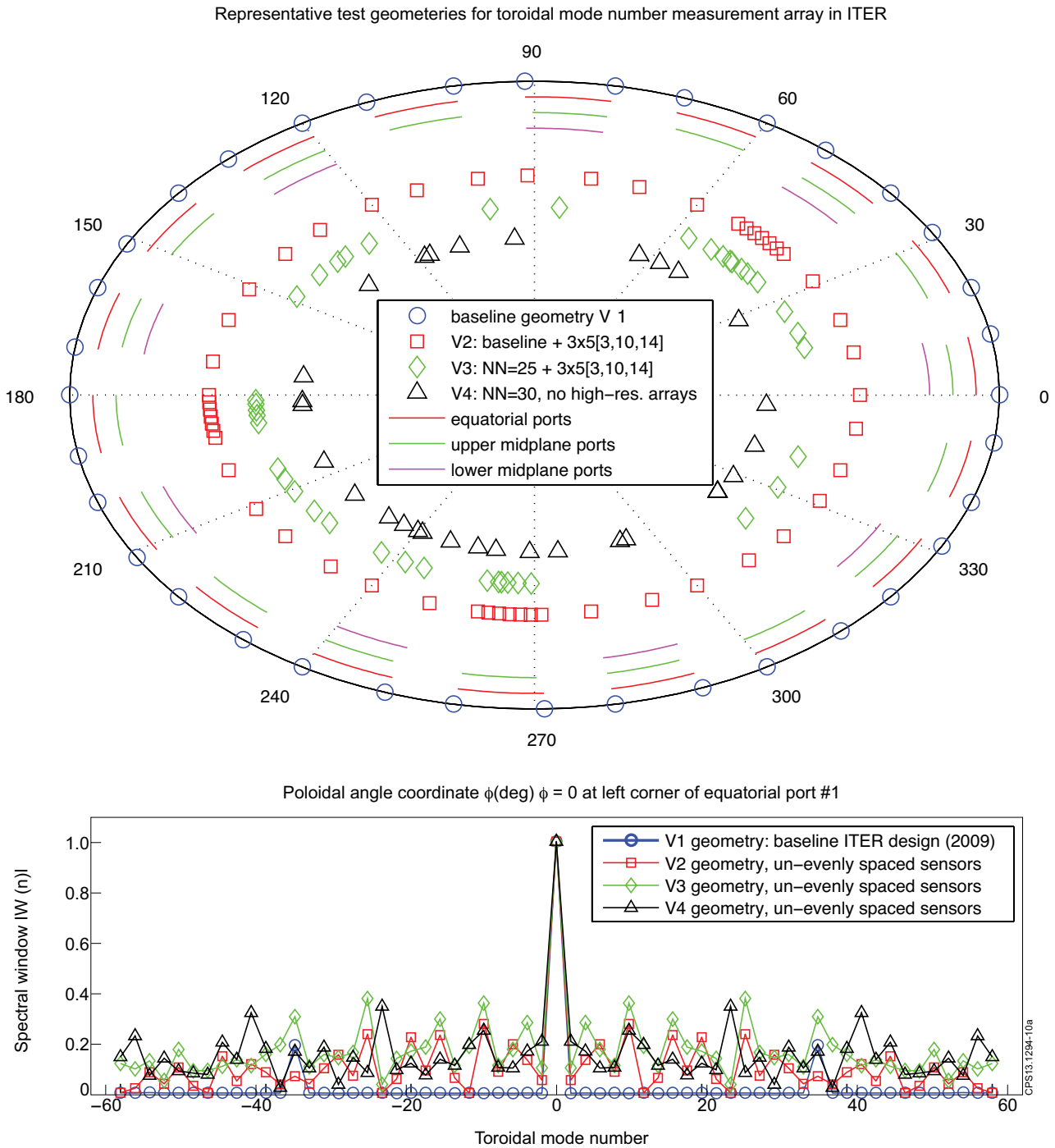

Figure 10a: Some representative examples of the test geometries used for the performance analysis for the ITER toroidal mode number measurement array. The baseline geometry (V1) represents the nominal ITER design as in 2009, with NN=2x18 equi-spaced sensors. The V2 geometry adds to this baseline design 3 arrays of 5 high-resolution sensors each in the equatorial ports [#3, #10, #14]. The V3 geometry replaces the NN=2x18 equi-spaced (baseline) sensors of the V2 geometry with NN=25 un-evenly spaced sensors. Finally, the V4 geometry uses NN=30 un-evenly spaced sensors without high-resolution arrays. Note that only the V1 geometry with equi-spaced sensors has W(ν)=0 exactly for all mode numbers except n=0 and the pseudo-Nyquist value $|n|=18$.

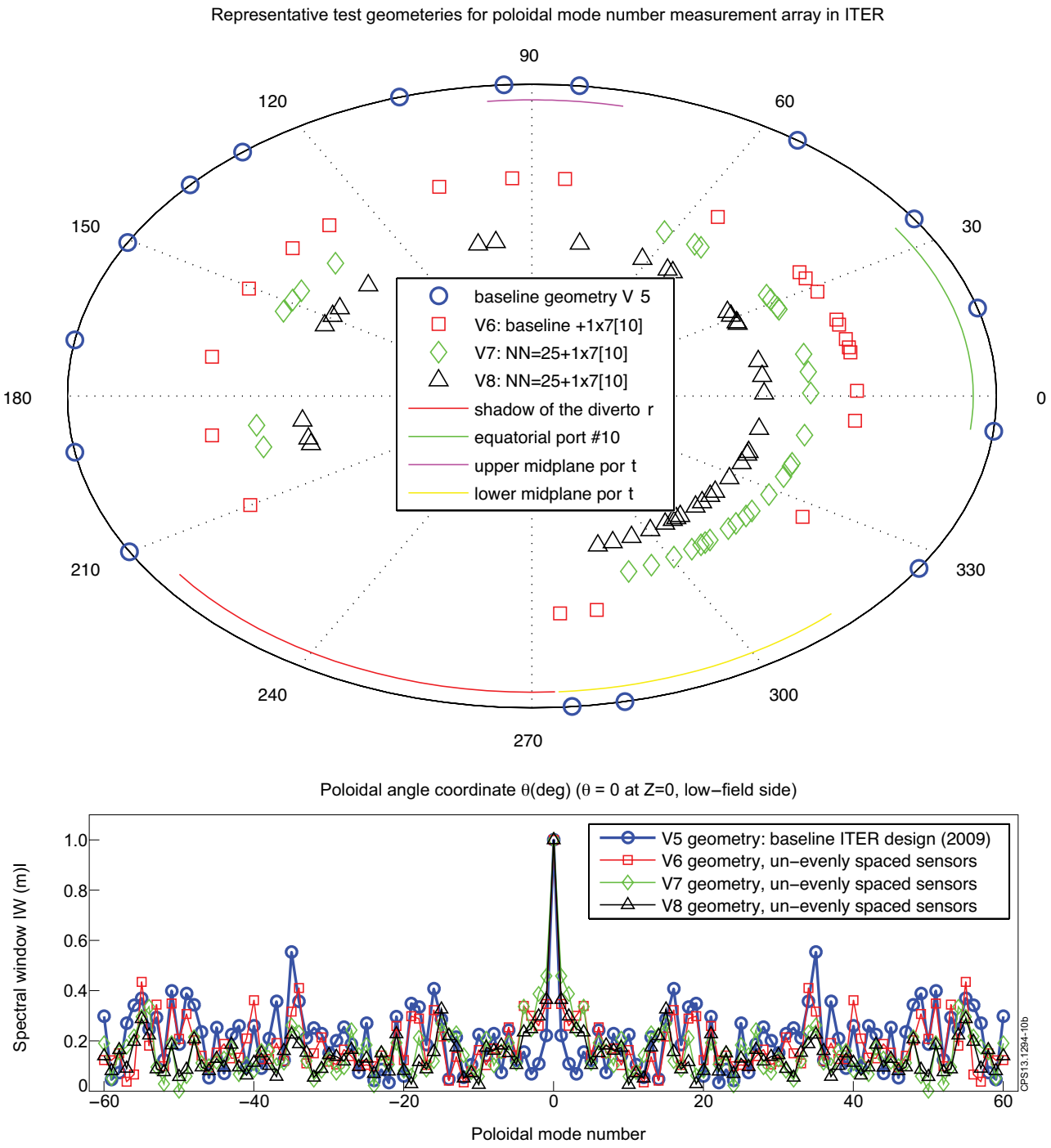

Figure 10b: Some representative examples of the test geometries used for the performance analysis for the ITER poloidal mode number measurement array. The baseline geometry (V5) represents the nominal ITER design as in 2009, with NN=16 un-evenly spaced sensors. The V6 geometry adds to this baseline design one array of 7 high-resolution sensors in the equatorial port [#10]. The V7 and V8 geometries replace the NN=16 baseline sensors of the V5 geometry with NN=25 un-evenly spaced sensors, but located at different test positions. As the sensors are not equi-spaced, no geometry has W(v)=0 exactly for any mode numbers.

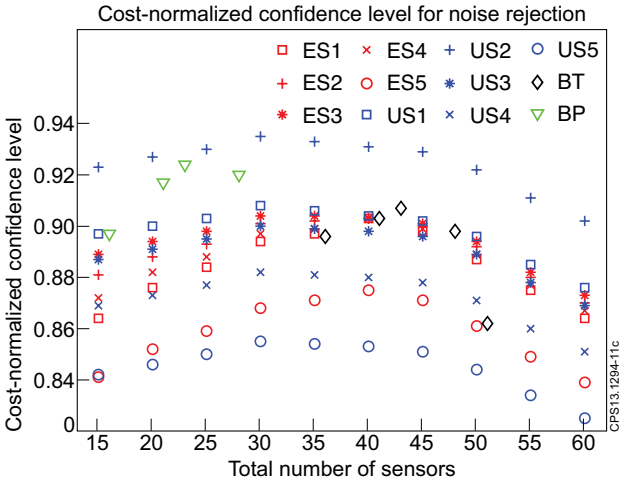

Figure 11: Cost-normalized confidence level for noise rejection for evenly (ES#) and un-evenly (US#) spaced sensors, comparing the data with the baseline toroidal (BT) and poloidal (BP) assemblies. The data are plotted as a function of the total number of sensors. We note a characteristic bell shape in the cost-normalized confidence level, which is obtained because above a certain number of sensors, the cost increases much more rapidly than the confidence level for noise rejection, which remains almost constant. The ES#, US#, BT and BP labels indicate different sensors' setups, as described in Section-4.

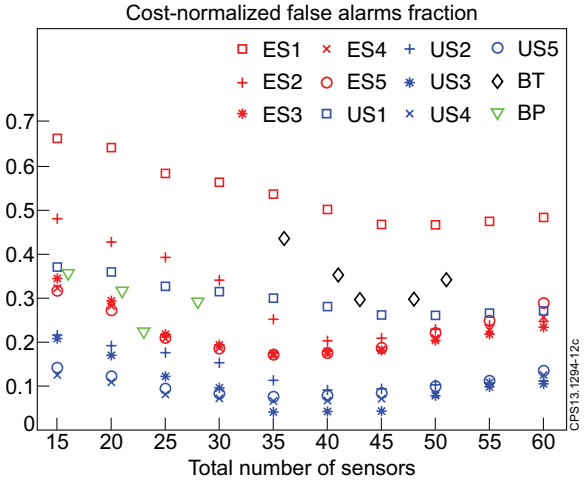

Figure 12: Cost-normalized false alarm fraction for evenly and un-evenly spaced geometries, and also comparing the results with those for the baseline toroidal and poloidal assemblies. The labeling format for the different geometries is the same as in fig11. We note again the characteristic (in this inverted up-down) bell shape in the cost-normalized fraction of false alarms, which is obtained because above a certain number of sensors, the cost increases much more rapidly than the false alarm rejection, which remains almost constant. For this analysis we used λ_{NORM}=0.85 and set f_{MAX} to be five times larger than the maximum physical mode number present in the input spectrum, i.e. $|f_{MAX}|$=150 and $|f_{MAX}|$=300 for toroidal and poloidal mode number analysis, respectively.

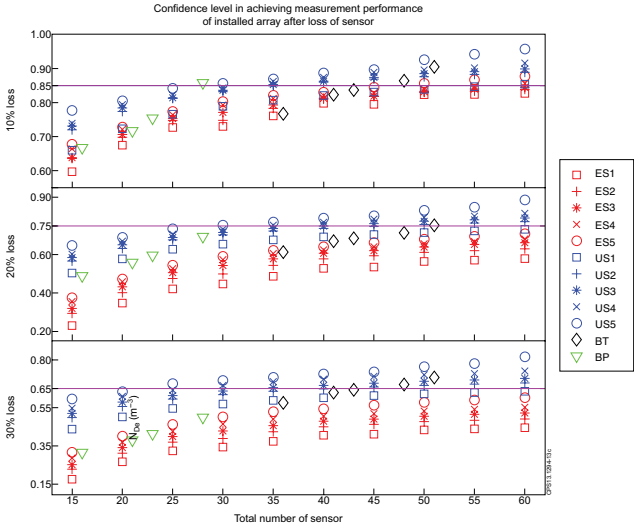

Figure 13: The confidence level in achieving the same measurement performance of the installed assembly after a [10%, 20%, 30%] loss of sensors. The labeling format for the different geometries is the same as in fig11. As in fig12, for this test we used λ_{NORM}=0.85 and $|f_{MAX}|$=150 and $|f_{MAX}|$=300 for toroidal and poloidal mode number analysis, respectively. The threshold values =0.85, =0.75 and =0.65 associated to a nominal [10%, 20%, 30%] loss of sensors, respectively, for acceptance of this test are explicitly shown by the horizontal (magenta) lines to guide the eye. For toroidal mode number analysis, the nominal ITER geometry satisfies the requirements for the resilience in the measurement performance when adding at least 1x12 high-resolution sensors, for a total of 48 sensors. Conversely, an assembly with 25 un-evenly spaced sensors in total, comprising 3x5 high-resolution arrays, satisfies these requirements. For poloidal mode number analysis, only an assembly with 30 to 35 un-evenly spaced sensors in total, comprising one array of 12 high-resolution sensors, satisfies the requirements for resilience in the measurement performance.

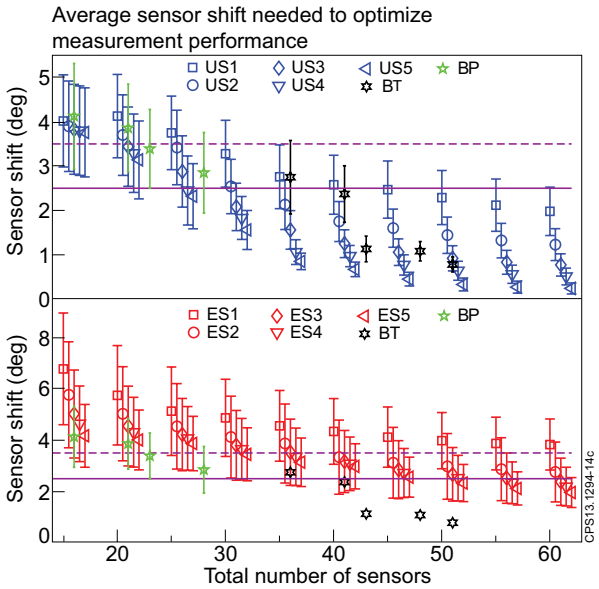

Figure 14: The average positional shift required to optimize the measurement performance given an initial sensors' arrangement. The horizontal axis is slightly displaced for the different geometries to improve the clarity of the graphical presentation, and the vertical error-bar indicates the standard deviation on the average value of the required sensor shift. The labeling format for the different geometries is the same as in fig11. As in fig12, for this test we used λ_{NORM}=0.85 and $|f_{MAX}|$=150 and $|f_{MAX}|$=300 for toroidal and poloidal mode number analysis, respectively. The threshold values =2.5deg and =3.5deg for acceptance of this test are explicitly shown by the horizontal (magenta) lines to guide the eye. We find that the nominal ITER geometry for toroidal mode number analysis satisfies the optimization requirements only when adding at least 1x7 high-resolution sensors, i.e. for a total of 43 sensors, whereas an assembly with 25 un-evenly spaced sensors in total, comprising 3x5 high-resolution arrays, satisfies these requirements. The nominal ITER geometry for poloidal mode number analysis does not satisfy the optimization requirements, whereas an assembly with 25 un-evenly spaced sensors in total, comprising 12 high-resolution sensors, satisfies them.

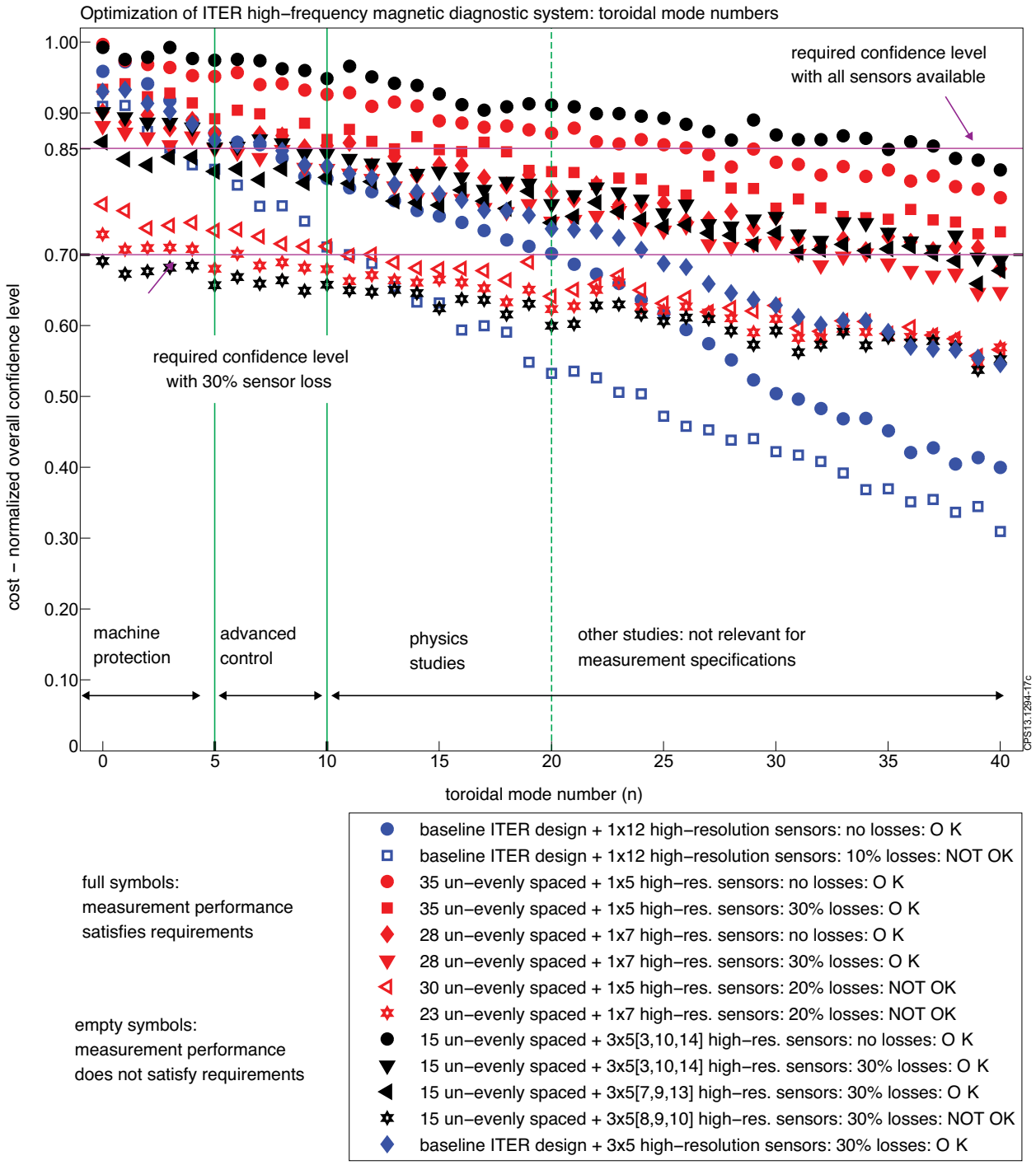

Figure 15a: Summary results of the measurement performance analysis for some representative geometries usable for toroidal mode number detection. The green vertical lines separate the mode numbers into classes, corresponding to different measurement requirements for HF instabilities in ITER. Similarly, the horizontal magenta lines reflect changing desiderata in the required confidence level. Both sets of lines can be moved to reflect changing physical understanding and measurement specifications.

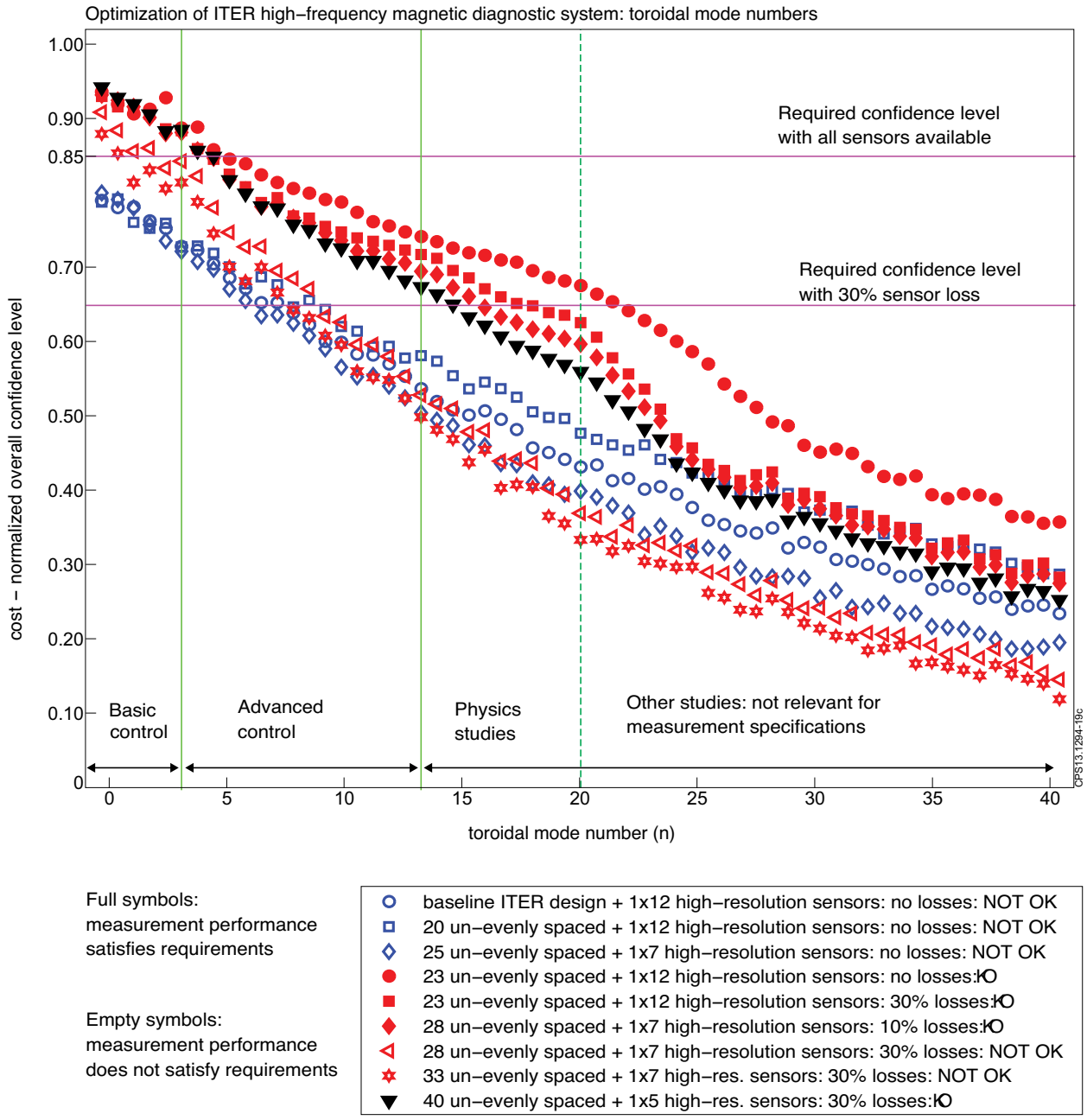

Figure 15b: Summary results of the measurement performance analysis for some representative geometries usable for poloidal mode number detection, using the same plotting format as in fig15a.